CrystEngComm

ROYAL SOCIETY OF CHEMISTRY

PAPER

View Article Online
View Journal | View Issue

Cite this: *CrystEngComm*, 2025, **27**, 3752

Mechanochemical synthesis and ^{35}Cl NMR crystallography of ionic cocrystals of phenothiazine drugs†

Zachary T. Dowdell, [ab] Austin A. Peach, [ab] John P. Purdie,[c] Sean T. Holmes, [ab] Lara K. Watanabe, [c] Jeremy M. Rawson [c] and Robert W. Schurko *[ab]

The solid forms of active pharmaceutical ingredients (APIs), such as polymorphs, cocrystals, and hydrates, possess unique physicochemical properties, including stability, bioavailability, and solubility. These properties are closely tied to their structures, which can be specifically tailored through rational design of novel forms. HCl salts are among the most common solid forms of APIs; however, the formation of pharmaceutical cocrystals of HCl APIs with pharmaceutically acceptable coformers, while relatively rare, can vastly expand the landscape of solid forms. This study explores the mechanochemical synthesis of known cocrystals of promethazine HCl and novel cocrystals of promethazine HCl and chlorpromazine HCl, along with the use of ^{35}Cl solid-state NMR (SSNMR) spectroscopy and density functional theory (DFT) calculations for their structural characterization. Mechanochemical synthesis methods were employed, offering higher yields and better scalability than conventional methods. However, the nature of the products of mechanochemical reactions, which are often powders, presents significant challenges for crystal structure determination. ^{35}Cl SSNMR experiments were used to reveal the chloride environments with distinct hydrogen bonding networks in each solid form, identified through unique quadrupolar interaction parameters. Experimental ^{35}Cl electric field gradient (EFG) tensor data were compared with those from DFT calculations, and used to identify a series of unique chloride ion hydrogen bonding configurations. This work highlights the potential of NMR crystallography for advancing the rational design of cocrystals, improving synthetic methodologies, and providing deeper insights into their solid-state properties.

Received 19th April 2025,
Accepted 28th April 2025

DOI: 10.1039/d5ce00426h

rsc.li/crystengcomm

1. Introduction

Approximately 80% of active pharmaceutical ingredients (APIs) are manufactured and administered as solids,[1] which can take on a multitude of solid forms such as salts, solvates, polymorphs, cocrystals, amorphous solid dispersions, and combinations thereof (*e.g.*, ionic cocrystals).[2] Currently, more than 50% of APIs are manufactured as solid, organic HCl salts, in which the chloride ions are involved in intricate hydrogen bonding networks that have been demonstrated to impart improved solubility and stability.[3,4] Each solid form of an API can have disparate physicochemical properties (*e.g.*, solubility, stability, bioavailability, *etc.*); as such, the ability to synthesize a variety of solid forms in high purity can permit the manufacture of more efficacious drugs with desirable properties, which is of paramount interest to the pharmaceutical industry as well as consumers of pharmaceutical products.

Pharmaceutical cocrystals, which are crystalline, single-phase materials composed of two or more distinct pharmaceutically acceptable molecules within a unit cell (not including hydrates, solvates, or simple salts),[5,6] are of particular interest due to the sheer number of coformers that can be used to elicit a wide range of structures and concomitant physicochemical properties.[7–9] Cocrystals are often formed *via* slow evaporation from solution;[6,10,11] however, this has several drawbacks, such as the use of relatively large volumes of solvents, high energy inputs, long waiting times (*e.g.*, weeks to months), and difficulties with scaling up output for industrial production.[12–18] Despite the widespread use of HCl salts of APIs and the significant potential for ionic cocrystal synthesis, studies on cocrystals of HCl APIs are surprisingly scarce, but are gaining much interest in pharmaceutical research, since they offer the

[a] *Department of Chemistry & Biochemistry, Florida State University, Tallahassee, FL, 32306, USA. E-mail: rschurko@fsu.edu*
[b] *National High Magnetic Field Laboratory, Tallahassee, FL 32310, USA*
[c] *Department of Chemistry and Biochemistry, University of Windsor, Windsor, ON, N9B 3P4, Canada*

† Electronic supplementary information (ESI) available: CCDC 2425375 and 2425376. For ESI and crystallographic data in CIF or other electronic format see DOI: https://doi.org/10.1039/d5ce00426h

enticing prospects of tailoring different solid forms with modified stability, solubility, or controlled release properties. However, their synthesis using conventional solution-based recrystallization is challenging, since they are often less likely to form, either because of preferred protonation of basic functional groups or less favorable thermodynamic properties, both of which often lead to the formation of a simple HCl salt.

Mechanochemistry offers alternative routes for cocrystal synthesis with quantitative yields, minimal impurities, short timescales (*i.e.*, minutes to hours), and straightforward scalability.[19–25] One of the most common mechanochemical synthetic techniques for small scale reactions is *ball milling*,[26–28] in which the reagents (or educts) are placed into a milling jar with ball bearings and ground at a specific frequency for a fixed duration.[27,29] A small amount of liquid can be used as well, typically no greater than 2 μL mg^{-1} of solid, to speed up or facilitate the reaction – this is known as *liquid assisted grinding* (LAG), while ball milling in the absence of solvent is referred to as *neat grinding* (NG).[30,31] The products and/or mixtures of species that emerge from ball milling reactions often come in the form of microcrystalline powders, which often restricts the application of single-crystal X-ray diffraction (SCXRD) methods (*i.e.*, crystals of suitable size and/or quality cannot be extracted). Fortunately, there are numerous other analytical techniques for characterizing the molecular structures of these products, with powder X-ray diffraction (PXRD), IR/Raman spectroscopy, and solid-state NMR (SSNMR) spectroscopy at the forefront. SSNMR spectroscopy is of particular value for its ability to resolve molecular structures in an atom-by-atom fashion, while also providing "fingerprints" for each solid form, akin to those of PXRD, IR, and Raman methods.

^{35}Cl (spin I = 3/2) SSNMR is well established for characterizing HCl APIs and their cocrystals, since spectra have broad, central transition (CT, +1/2 ↔ −1/2) powder patterns that are tens to hundreds of kHz in breadth, due to influences from the second-order quadrupolar interaction (SOQI) and chemical shift anisotropy (CSA).[32–41] The quadrupolar interaction is the interaction between the nuclear quadrupole moment and the electric field gradient (EFG) at the nucleus, the latter of which is described by a second-rank tensor. Measurement of ^{35}Cl EFG tensors is especially useful for characterizing chloride ion environments, since they are very sensitive to their local ground-state electronic environments and can distinguish even minute differences or changes between hydrogen bonding networks.[3,42–44] With the aid of dispersion-corrected density functional theory (DFT) geometry optimizations and computation of ^{35}Cl EFG tensors, further insight into the molecular-level structures of materials without known crystal structures can be gained.[32,45,46]

Given the relative scarcity of ionic HCl cocrystals of APIs and their potential importance in the design of new solid forms with useful physicochemical properties, herein, we discuss mechanochemical syntheses of eleven such cocrystals featuring the phenothiazine drugs promethazine HCl (**Ptz**), chlorpromazine HCl (**Cpz**), or promazine HCl (**Pmz**) (Scheme 1) and a series of neutral coformers (see ESI,† Scheme S1) as starting reagents, which yield 2 : 1 promethazine HCl : fumaric acid (**Ptz$_2$F**), 2 : 1 promethazine HCl : succinic acid (**Ptz$_2$S**), 2 : 1 promethazine HCl : adipic acid (**Ptz$_2$A**), 2 : 1 promethazine HCl : oxalic acid (**Ptz$_2$O**), 2 : 1 promethazine HCl : glutaric acid (**Ptz$_2$G**), 1 : 1 promethazine HCl : malonic acid (**PtzMo**), 1 : 1 promethazine HCl : malic acid (**PtzMi**), 2 : 1 chlorpromazine HCl : succinic acid (**Cpz$_2$S**), 2 : 1 chlorpromazine HCl : fumaric acid (**Cpz$_2$F**), and 1 : 1 chlorpromazine HCl : terephthalic acid (**CpzT**) (see Scheme 2 for examples). We demonstrate (i) the advantages of mechanochemical methods over previously reported synthetic procedures, (ii) the optimization of mechanochemical syntheses to maximize efficiency and yield, (iii) the application of these optimized protocols for the discovery of novel cocrystals, and (iv) the use of ^{35}Cl SSNMR to investigate the structures of known **Ptz** cocrystals,[32] and to aid in the structural elucidation of the novel **Ptz** and **Cpz** cocrystals, *via* NMR crystallography (NMRX).[47–49] Lastly, experimental ^{35}Cl EFG tensors are compared to those calculated from structural models that have been geometry optimized using dispersion-corrected plane-wave DFT methods.[46] This helps assess how ^{35}Cl EFG tensors of chloride ions are influenced by hydrogen bonding networks, which is key for future applications of quadrupolar NMR-guided crystallographic crystal structure prediction methods to HCl APIs.[50,51]

2. Methods

2.1 Materials

Promethazine HCl (**Ptz**), chlorpromazine HCl (**Cpz**), promazine HCl (**Pmz**), and coformers succinic acid (**S**), oxalic

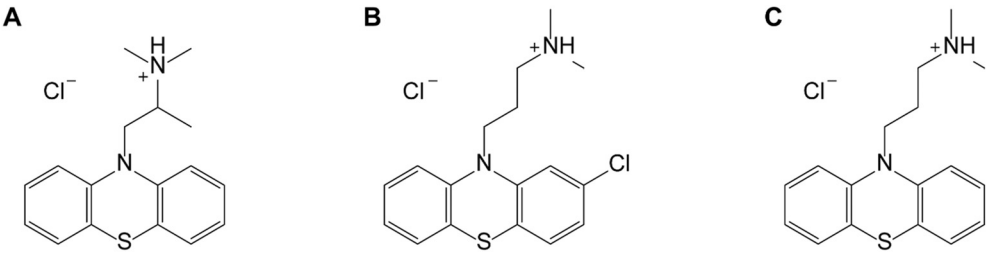

Scheme 1 Molecular structures of (A) promethazine HCl (**Ptz**), (B) chlorpromazine HCl (**Cpz**), and (C) promazine HCl (**Pmz**).

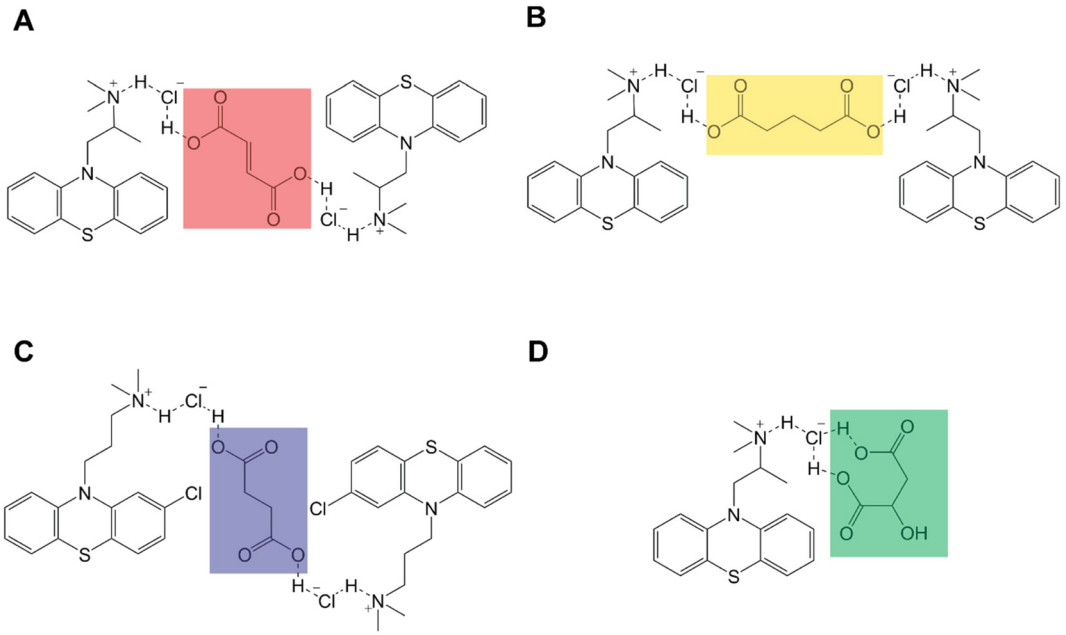

Scheme 2 Schematic molecular structures of (A) promethazine HCl : fumaric acid 2 : 1 cocrystal (**Ptz$_2$F**), (B) promethazine HCl : glutaric acid 2 : 1 cocrystal (**Ptz$_2$G**), (C) chlorpromazine HCl : succinic acid 2 : 1 cocrystal (**Cpz$_2$S**), and (D) promethazine HCl : malic acid 1 : 1 cocrystal (**PtzMi**). The coformers fumaric acid, glutaric acid, succinic acid, and malic acid are highlighted in red, yellow, blue, and green respectively.

acid (**O**), malonic acid (**Mo**), malic acid (**Mi**), glutaric acid (**G**), adipic acid (**A**), terephthalic acid, (**T**) and fumaric acid (**F**), were purchased from Millipore Sigma and used as received without further purification. PXRD patterns were acquired for all starting reagents and compared to simulated PXRD patterns of known structures to assess identity and purity.

2.2 Cocrystal synthesis

Cocrystals were synthesized using slow evaporation and/or mechanochemically *via* ball milling. Initial mechanochemical syntheses were carried out following the procedures reported by Borodi *et al.*[10] Mechanochemical syntheses involved either LAG or NG, and were conducted using a Retsch Mixer Mill 400 using two 15 mL stainless steel jars with two 7 mm stainless steel grinding balls, a milling frequency of 30 or 35 Hz, and milling times ranging from 5 to 360 minutes (Tables 1 and 2). No further grinding of samples was needed prior to analyses by SSNMR or PXRD, since all were produced as fine, microcrystalline powders. For syntheses of cocrystals *via* slow evaporation, supersaturated solutions were prepared in a 20 mL glass vial by dissolving one of three APIs and one of the eight coformers in 2 mL of acetonitrile (MeCN), with gentle heating (*ca.* 55 °C) to completely dissolve the solids. The solutions were placed in a fume hood to evaporate over a period of 5 days (see Table 3 for details). The resulting crystals were analyzed by SCXRD.

2.3 Powder X-ray diffraction

PXRD patterns were acquired on a Rigaku Miniflex with a Cu Kα (λ = 1.540593 Å) radiation source and a HyPix-400 MF 2D hybrid pixel array detector. The X-ray tube voltage and amperage were set to 40 kV and 15 mA. Experiments were run with the detector scanning 2θ angles from 5° to 50° with a step size of 0.03° at a speed of 5° min^{-1}. The PXRD patterns for all reagents and cocrystals were compared to those simulated from reported structures[10,52–56] using CrystalDiffract software,[57] to confirm crystallinity, purity, and the presence of novel phases.

Table 1 Mechanochemical parameters for the preparation of previously reported **Ptz** pharmaceutical cocrystals

Cocrystal	Original milling time[a] (minutes) at 27 Hz	Optimized milling time[b] (minutes) at 30 Hz	Acetonitrile added for optimized milling[b] (μL)
Ptz$_2$F	90	30	20
Ptz$_2$S	n/a	5	15
Ptz$_2$O	180	5	15
Ptz$_2$A	90	10	10

[a] Reported by Borodi *et al.*, unspecified amount of solvent, see ref. 10. [b] Reported in this work.

Table 2 Mechanochemical parameters for the preparation of novel **Ptz** and **Cpz** pharmaceutical cocrystals

Cocrystal	Milling time (minutes) at 30 Hz	Milling time[a] (minutes) at 35 Hz	Acetonitrile[b] (μL)
PtzMo	30	15	20
PtzMi	10	5	10
Ptz_2G	360	180	5
Cpz_2S	30	15	15
CpzT	30	15	10
Cpz_2F	30	15	10

[a] Ball milling at a rate of 35 Hz was carried out using an MM500 Vario, further optimizations were not attempted. [b] Small amounts of acetonitrile were added to aid in liquid assisted grinding (LAG), the same amount of acetonitrile was used for syntheses at both milling rates of 30 and 35 Hz.

Table 3 Synthetic parameters for novel **Cpz** pharmaceutical cocrystals formed *via* slow evaporation

Cocrystal	Mass of API (mg)	Mol of API (mmol)	Mass of coformer (mg)	Mol of coformer (mmol)	Acetonitrile added (mL)	Time for suitable crystals (days)
Cpz_2F	61	0.17	12	0.10	2	5
Cpz_2S	62	0.17	11	0.09	2	5

2.4 Single-crystal XRD

Single crystals of **CpzF** and **CpzS** were mounted on a cryoloop with paratone oil and examined on a Bruker Dual Source D8 Venture diffractometer equipped with Photon 100 CCD area detector using graphite monochromated Mo-Kα radiation (λ = 0.71073 Å). An Oxford Cryostream cooler was used to maintain cryogenic temperatures of 170 K for these studies. Data were collected using the APEX-III software, integrated using SAINT[58] and corrected for absorption using a multi-scan approach (SADABS).[59] Final cell constants were determined from full least squares refinement of all observed reflections. The structures were solved using intrinsic phasing (SHELXT)[60] and refined with full least squares refinement on F^2 using SHELXL[61] in Olex2–1.5 software.[62] Simulated PXRD patterns derived from the single-crystal structures were found to be identical to those of the bulk, microcrystalline samples.

2.5 Solid-state NMR spectroscopy

2.5.1 Overview. SSNMR experiments at B_0 = 9.4 T [$\nu_0(^1H)$ = 400.13 MHz and $\nu_0(^{35}Cl)$ = 39.21 MHz] were conducted on a Bruker Avance III HD NMR spectrometer with an Oxford wide-bore magnet at the University of Windsor. SSNMR experiments at B_0 = 14.1 T [$\nu_0(^1H)$ = 600.13 MHz and $\nu_0(^{13}C)$ = 150.92 MHz] and B_0 = 18.8 T [$\nu_0(^1H)$ = 800.13 MHz and $\nu_0(^{35}Cl)$ = 78.42 MHz] were conducted on Bruker Avance NEO spectrometers with 89 mm and 63 mm bore Oxford magnets, respectively, at the National High Magnetic Field Laboratory (NHMFL). SSNMR experiments at 9.4 T were conducted with a 5 mm ultra-low temperature, double-resonance HX static (stationary sample) NMR probe manufactured by Revolution NMR, with samples packed into 5 mm outer diameter (o.d.) glass NMR tubes sealed with Teflon tape. Magic-angle spinning (MAS) and static SSNMR experiments at 14.1 T and 18.8 T were carried out with 5 mm, 3.2 mm, and/or 1.3 mm triple resonance HXY probes built in-house at the NHMFL, with samples packed into 3.2 or 1.3 mm o.d. zirconia oxide rotors (MAS) or 5 mm o.d. glass sample holders (static). Details of these experiments are provided in Tables S1–S7.† Pulse sequences and recommended standards and calibration parameters are available at **https://github.com/rschurko**.

2.5.2 ^{35}Cl SSNMR. Static ^{35}Cl SSNMR spectra were obtained at both 9.4 T and 18.8 T, while MAS spectra were acquired only at 18.8 T. At 9.4 T, spectra were obtained using the WURST-CPMG[63–66] pulse sequence with a ^{1}H continuous-wave (CW) decoupling field between 25 and 50 kHz. At 18.8 T, static spectra were obtained using either a Hahn Echo or CPMG pulse sequence with a CW ^{1}H decoupling field of 50 kHz. MAS spectra at 18.8 T were obtained using a rotor-synchronized quadrupolar echo sequence, with an MAS rate of ν_{rot} = 50 kHz.[67] ^{35}Cl chemical shifts were referenced to 0.1 M NaCl at δ_{iso} = 0 ppm using NaCl(s) as a secondary reference (δ_{iso} = −41.1 ppm).

2.5.3 ^{13}C SSNMR. ^{1}H–^{13}C variable-amplitude cross polarization/MAS (VACP/MAS) experiments[68–72] were conducted at ν_{rot} = 10 kHz. Data were acquired using a 5.0 μs ^{1}H π/2 pulse, a ramped-amplitude Hartman–Hahn matching field of $\nu_2(^1H)$ = 50 kHz (matched on the X channel),[69] optimized contact times between 1.0 and 3.0 ms, and a SPINAL-64 ^{1}H decoupling field of $\nu_2(^1H)$ = 50 kHz.[73] ^{13}C chemical shifts were referenced to TMS (δ_{iso} = 0.0 ppm) using α-glycine (δ_{iso} = 176.5 ppm) as a secondary reference.[74,75]

2.5.4 Spectral processing and simulation. SSNMR spectra were processed using TopSpin v4.1 software package. Simulations of ^{35}Cl SSNMR spectra were generated using the ssNake v1.3 software package.[76] To ensure proper expression of the Euler angles describing the relative orientation of the EFG and CS tensors in the *ZY′Z″* convention, the results of simulations in ssNake, which uses the *ZX′Z″* convention and different definitions for

anisotropic chemical shift and EFG tensor parameters, were verified in WSolids1.[77]

2.6 DFT calculations

Quantum chemical calculations were performed on structural models obtained from previous SCXRD studies,[10,52,53,56] or the two novel cocrystals obtained through SCXRD analyses presented herein. Geometry optimizations and subsequent calculations of ^{35}Cl EFG and magnetic shielding tensors were performed with plane-wave DFT methods using the CASTEP module within Materials Studio 2020.[78,79] These calculations used the generalized gradient approximation (GGA) with the RPBE functional,[80] ultrasoft pseudopotentials generated on-the-fly,[81] a *k*-point spacing of 0.05 Å^{-1}, a plane-wave cut-off energy of 800 eV, and an SCF convergence threshold of 5×10^{-7} eV. Geometry optimizations employed the LBFGS method,[82] in which the positions of all atoms were relaxed with unit cell parameters remaining fixed at their experimental values. The thresholds for structural convergence included a maximum change in energy of 5×10^{-6} eV per atom, a maximum displacement of 5×10^{-4} Å per atom, and a maximum Cartesian force of 10^{-2} eV Å^{-1}. A correction to the dispersion energy was introduced using Grimme's semi-empirical two-body dispersion force field,[83,84] with an empirical reparameterization introduced by our group (DFT-D2*).[46,85–88] ^{35}Cl magnetic shielding tensors were calculated using the GIPAW method.[89] ^{35}Cl chemical shift values were referenced with respect to NaCl(s) (δ_{iso} = −41.1 ppm), which has an absolute isotropic chemical shielding value of 952.38 ppm. EFGShield[90] was used to extract the Euler angles describing the relative orientations of magnetic shielding and EFG tensors, which are reported using the *ZY′Z″* convention.

3. Results and discussion

3.1 Overview

In this section, we discuss (i) the optimized mechanochemical syntheses of previously reported **Ptz** cocrystals; (ii) the optimized mechanochemical syntheses of novel **Ptz** and **Cpz** cocrystals with various coformers; (iii) the characterization of these cocrystals using a combination of SSNMR, PXRD, and SCXRD; and (iv) the use of DFT calculations to gain insight into relationships between ^{35}Cl EFG tensors and molecular-level structure, as well as the application of NMRX methods for the preliminary characterization of materials without known crystal structures. All cocrystals were characterized by SSNMR; in particular, ^{35}Cl SSNMR is highlighted as the central characterization method due to the unique ^{35}Cl central transition (CT, +1/2 ↔ −1/2) powder patterns resulting from the multifarious hydrogen bonding arrangements of the Cl$^-$ anions in both the HCl APIs and their cocrystals. For cocrystals with known crystal structures, DFT-D2* geometry optimizations and calculations of ^{35}Cl EFG tensors are used to correlate the ^{35}Cl EFG tensor parameters and orientations to the local hydrogen bonding environments of the chloride ions – this is crucial for understanding the roles of the chloride ions in stabilizing these novel ionic cocrystals.

3.2 General observations

Mechanochemical syntheses. In 2019 Borodi *et al.* reported the syntheses of four **Ptz** cocrystals, including **Ptz$_2$F**, **Ptz$_2$S**, **Ptz$_2$A**, and **Ptz$_2$O**, using mechanochemistry and/or slow evaporation, using **Ptz** and a neutral coformer as the starting reagents.[10] LAG reactions with an unspecified amount of solvent were reported to take between 30 to 90 minutes to produce quantitative yields of cocrystals, while analogous NG reactions took 180 minutes. However, the type and amount of solvent used in LAG syntheses, along with the ball milling conditions, can have a significant impact on both the efficiency and yield of the reaction. Following Friščić and co-workers,[91] our syntheses were optimized using the following ball milling conditions: (i) a series of different LAG solvents were explored, including ethanol, methanol, water, acetonitrile, diethyl ether, THF, nitromethane, dichloromethane, and toluene; (ii) the LAG solvent volume to total educt mass ratio was in the range of 5–20 μL of solvent per 200 mg of solid; (iii) the milling time was varied between 5 and 360 minutes; and (iv) the milling frequency was set to 30 or 35 Hz (Table 1). Furthermore, we were able to produce the **Ptz$_2$S** cocrystal under mechanochemical conditions, which was not reported previously.

The optimized ball milling protocols served as a starting point for the syntheses or attempted syntheses of novel cocrystals with **Ptz**, **Cpz**, and **Pmz** as starting reagents. Six new cocrystals were synthesized, including three with **Ptz** and three with **Cpz**. Most of these cocrystals can be synthesized in less than 30 minutes under LAG conditions, with the exception of **Ptz$_2$G**, which takes six hours of milling before formation of the cocrystal is completed (Table 2). Attempts to synthesize other novel cocrystals of **Ptz**, **Cpz**, and **Pmz** with different coformers (*i.e.*, tartaric acid, salicylic acid, benzoic acid, benzamide, gentisic acid, xinafoic acid, maleic acid, and aspartic acid) were unsuccessful, despite efforts with various stoichiometric ratios to API to coformer, solvent identity and volume, milling media (*i.e.*, stainless steel and Teflon), and milling times (*e.g.*, 30 minutes and up to five hours). Details on attempts to produce **Pmz** cocrystals are reported in Table S8.†

Powder X-ray diffraction. PXRD patterns of reported **Ptz** cocrystals are distinct from those of the starting reagents (Fig. S1†) and in good agreement with simulated patterns based on crystal structures (Fig. S2†). PXRD patterns of the novel cocrystals **Cpz$_2$F** and **Cpz$_2$S** are compared with simulated patterns (Fig. S3†) based on the crystal structures reported herein (*vide infra*, Table S9†). PXRD patterns of novel cocrystals without known crystal structures are compared to patterns of educts (Fig. S4 and S5†), with key diffraction peaks attributed to a novel phase, and compared to simulated patterns derived from the novel structures

reported herein. These results confirm that the syntheses are successful, the products are crystalline with no presence of impurities, and the bulk powders are of the same phase as larger crystals.

Single-crystal X-ray diffraction. Slow evaporations were attempted in hopes of obtaining crystals suitable for analysis by SCXRD; however, only recrystallizations of **Cpz$_2$F** and **Cpz$_2$S** have been successful to date. These cocrystals are isostructural, crystallizing in the monoclinic space group $C2/c$, each featuring a single, crystallographically unique chloride ion site (Table S9 and Fig. S6†). These crystal structures are available from the Cambridge Structural Database under deposition numbers 2 425 375 (**Cpz$_2$F**) and 2 425 376 (**Cpz$_2$S**).

^{13}C SSNMR. The formation of distinct intermolecular hydrogen bonding arrangements in the cocrystals, as evidenced by ^{13}C SSNMR spectra, highlights key structural differences from the **Ptz**, **Cpz**, and coformer educts. The ^{13}C SSNMR spectra of the educts and cocrystals feature peaks with full widths at half height of ≤3 ppm (Fig. S7–S9†). Comparison of the ^{1}H–^{13}C CP/MAS NMR spectra of the cocrystals and educts reveals marked differences in the δ_{iso} values of certain carbon peaks – notably, the peaks corresponding to the carbonyl carbons and carbons directly bound to the protonated nitrogen atoms in both **Ptz** and **Cpz** are distinct from those of the corresponding cocrystals (see Tables S10–S12† for assignments of δ_{iso}(^{13}C) values). These differences likely arise from distinct intermolecular hydrogen bonding arrangements involving the API and coformer molecules, where the bond lengths between the hydrogen atom on the tertiary amine and the Cl$^-$ ion (R′R$_2$NH$^+$···Cl) in **Ptz** and **Ptz** cocrystals have differences of roughly 0.1 Å (Table 4). Interestingly, **Ptz$_2$G** stands out as possibly being disordered, indicated by the doubled glutaric acid peaks at around 174–175 ppm and the two **Ptz** peaks corresponding to methyl carbon #9 at 10 and 8 ppm as well as carbon #6 at 144 and 143 ppm (Table S10†). In the crystal structure of **Ptz$_2$A**, carbon #9 is near the carbonyl carbon—this is likely also the case in **Ptz$_2$G**. Due to the small change in chemical shift (<1 ppm) of just a single carbon in the glutaric acid component, a similar change in carbon #6 in the **Ptz** component, and a slightly larger change in chemical shift of carbon #9 (~1.5 ppm) in the **Ptz** component, we believe carbon #9 is disordered, which leads to a small changes in these nearby carbons.

3.3 ^{35}Cl SSNMR

^{35}Cl SSNMR spectra were acquired for all APIs and cocrystals under static conditions at two magnetic fields, 9.4 T and 18.8 T, as well as under MAS conditions at 18.8 T for some materials (even at 18.8 T, certain samples with large magnitudes of C_Q are not amenable to MAS NMR experiments). These data aid in the accurate determination of both the CS and EFG tensors (Table 5), since the effects of

Table 4 List of H···Cl$^-$ contacts and calculated ^{35}Cl SSNMR parameters for APIs and cocrystals, as determined from X-ray diffraction derived crystal structures

Material	Contact type[a]	H···Cl$^-$ distance[b] (Å)	X···Cl$^-$ distance[c] (Å)	X–H···Cl$^-$ angle[d] (°)	X$_1$–Cl$^-$–X$_2$ angle[e] (°)	C_Q[f] (MHz)	η_Q[f]
APIs with a single H···Cl$^-$ short contact							
Ptz	RR′R″NH$^+$···Cl$^-$	1.964	2.969	173.8	n/a	−5.88	0.21
Cpz	RR′R″NH$^+$···Cl$^-$	2.035	3.024	169.9	n/a	−4.91	0.20
Pmz	RR′R″NH$^+$···Cl$^-$	2.001	2.994	171.0	n/a	−4.79	0.38
Cocrystals with two H···Cl$^-$ short contacts (type 1)							
Ptz$_2$F	ROOH···Cl$^-$	2.033	2.975	169.2	154.1	−9.90	0.08
	RR′R″NH$^+$···Cl$^-$	2.055	3.045	174.1			
Ptz$_2$S	RR′R″NH$^+$···Cl$^-$	2.053	3.046	175.1	152.0	−9.47	0.11
	ROOH···Cl$^-$	2.068	3.006	168.9			
Ptz$_2$A	RR′R″NH$^+$···Cl$^-$	2.039	3.034	177.5	156.8	−9.00	0.19
	ROOH···Cl$^-$	2.087	3.027	169.9			
Cocrystals with two H···Cl$^-$ short contacts (type 2)							
Ptz$_2$O	ROOH···Cl$^-$	2.029	2.975	168.6	99.8	5.19	0.13
	RR′R″NH$^+$···Cl$^-$	2.065	3.050	169.6			
Cpz$_2$F	ROOH···Cl$^-$	2.068	3.002	166.8	101.4	5.03	0.52
	RR′R″NH$^+$···Cl$^-$	2.093	3.069	167.3			
Cpz$_2$S	ROOH···Cl$^-$	2.051	2.990	167.6	102.1	5.24	0.53
	RR′R″NH$^+$···Cl$^-$	2.094	3.075	169.5			

[a] Indicates the functional group involved in the H···Cl$^-$ bond (*i.e.*, ROOH···Cl$^-$ signifies a carboxylic acid and RR′R″NH···Cl$^-$ signifies a charged tertiary amine contact). [b] The shortest H···Cl$^-$ hydrogen bonds (<2.6 Å), as determined *via* energy minimization and geometry optimization with DFT plane wave calculations. [c] The distance between the chloride ion and the hydrogen-bond donor atom (X = N, O). [d] Angle between the hydrogen-bond donor atom (X = N, O), the hydrogen atom, and the chloride ion. [e] Angle between the first short contact atom (X$_1$), the chloride ion, and the second short contact atom (X$_2$). [f] DFT calculations yield the sign of the quadrupolar coupling constant, C_Q, which is unobtainable from ^{35}Cl SSNMR experiments. It is noted that since Q(^{35}Cl) = −8.165 fm^2, positive and negative values of C_Q correspond to negative and positive EFGs, respectively. Definitions of C_Q and η_Q are given in Table 5.

Table 5 ^{35}Cl EFG and chemical shift tensor parameters obtained from experimental measurements and DFT calculations on DFT-D2* geometry-optimized structures[a–e]

Material		C_Q[b] (MHz)	η_Q[b]	δ_{iso}[c] (ppm)	Ω[c] (ppm)	κ[c]	α[d] (°)	β[d] (°)	γ[d] (°)
Ptz	Exp	6.49(4)	0.25(2)	66(9)	n/a[e]	n/a[e]	n/a[e]	n/a[e]	n/a[e]
	DFT	−5.88	0.21	52	17	0.07	28	12	62
Cpz[a]	Exp	5.66(5)	0.23(3)	41(2)	n/a[e]	n/a[e]	n/a[e]	n/a[e]	n/a[e]
	DFT	−4.91	0.20	34	73	0.01	13	19	189
Pmz	Exp	5.11(5)	0.23(2)	60(6)	72(30)	n/a[e]	152(20)	0(45)	0(45)
	DFT	−4.79	0.38	55	101	0.16	214	13	189
Ptz$_2$F[a]	Exp	9.42(7)	0.09(2)	14(2)	184(40)	0.3(2)	90(10)	4(8)	27(20)
	DFT	−9.90	0.08	44	118	0.48	45	14	130
Ptz$_2$S[a]	Exp	9.41(5)	0.09(2)	44(1)	90(20)	0.55(20)	45(15)	10(10)	30(30)
	DFT	−9.47	0.11	34	116	0.55	38	14	132
Ptz$_2$O[a]	Exp	5.07(5)	0.20(2)	39(2)	85(10)	n/a[e]	65(12)	80(5)	15(7)
	DFT	5.19	0.13	36	78	−0.25	69	87	172
Ptz$_2$A[a]	Exp	8.9(1)	0.15(2)	42(2)	100(20)	−0.7(3)	60(5)	10(10)	60(10)
	DFT	−9.00	0.19	36	118	0.58	55	10	102
PtzMo	Exp	8.64(5)	0.20(2)	10(10)	n/a[e]	n/a[e]	n/a[e]	n/a[e]	n/a[e]
PtzMi[a]	Exp	4.4(1)	0.62(4)	70(2)	150(20)	−0.5(4)	85(15)	75(20)	20(10)
Ptz$_2$G	Exp	8.8(1)	0.12(2)	31(8)	100(20)	0.7(3)	n/a[e]	25(10)	n/a[e]
Cpz$_2$S[a]	Exp	4.95(5)	0.57(4)	38(2)	150(30)	−0.6(3)	90(15)	90(10)	0(10)
	DFT	5.24	0.53	30	89	−0.11	129	88	182
Cpz$_2$F[a]	Exp	5.13(5)	0.51(2)	42(2)	100(20)	−0.7(4)	90(20)	90(20)	0(10)
	DFT	5.03	0.52	36	89	−0.10	137	87	180
CpzT[a]	Exp	4.50(8)	0.10(2)	27(1)	65(15)	−0.8(2)	85(25)	90(15)	0(10)

[a] ^{35}Cl SSNMR spectra were also acquired under MAS conditions for these samples. [b] The principal components of the EFG tensors are defined such that $|V_{33}| \geq |V_{22}| \geq |V_{11}|$. The quadrupolar coupling constant and asymmetry parameter are given by $C_Q = eQV_{33}/h$, and $\eta_Q = (V_{11} - V_{22})/V_{33}$, respectively. The sign of C_Q cannot be determined from the experimental ^{35}Cl spectra. [c] The principal components of the chemical shift tensors are defined using the frequency-ordered convention, with $\delta_{11} \geq \delta_{22} \geq \delta_{33}$. The isotropic chemical shift, span, and skew are given by $\delta_{iso} = (\delta_{11} + \delta_{22} + \delta_{33})/3$, $\Omega = \delta_{11} - \delta_{33}$, and $\kappa = 3(\delta_{22} - \delta_{iso})/\Omega$, respectively. [d] The Euler angles α, β, and γ define the relative orientation of the EFG and chemical shift tensors using the *ZY′Z″* convention for rotation. The experimental angles derived from ssNake (which uses the *ZX′Z″* convention) are adjusted to match the calculated values extracted by EFGShield. See ref. 90. [e] This parameter is not reported since it has little to no effect on the appearance of simulated powder patterns.

the CSA and SOQI on the CT patterns scale proportional and inversely proportional to the magnitude of B_0, respectively. MAS can completely or partially average the contributions from CSA, but only partially average the SOQI contributions; this enables facile determination of the quadrupolar coupling constant, asymmetry parameter, and isotropic chemical shift (C_Q, η_Q, and δ_{iso}, respectively) and simplifies simulations of corresponding static NMR spectra (the latter require eight parameters to fit, including the CS tensor parameters and Euler angles that describe the relative orientation of the EFG and CS tensors; see Table 5 for definitions of these parameters).

Unlike the ^{13}C SSNMR spectra, which appear quite similar to one another, the ^{35}Cl SSNMR patterns for each solid form are markedly different (*cf.* Fig. 1–4). This is due to the great sensitivity of the ^{35}Cl EFG tensors to the local hydrogen-bonding environments of the chloride ions. The ^{35}Cl spectra of each API and cocrystal feature a unique CT patterns that can be simulated to yield distinct sets of quadrupolar and chemical shift parameters (Table 5). The former are easily interpretable in terms of electronic structure: the absolute magnitudes of C_Q reflect the degree of spherical symmetry of the ground state electron density about the Cl$^-$ ion (increased magnitudes indicate less spherical symmetry), while the η_Q values describe the axial asymmetry of the EFG tensor (*i.e.*, $0 \leq \eta_Q \leq 1$, where $\eta_Q = 0$ is perfectly axial). All of this, combined with the relatively rapid acquisition times (Tables S1–S5†), makes ^{35}Cl SSNMR an ideal technique for obtaining spectral fingerprints and studying the relationships between the ^{35}Cl EFG tensors and hydrogen bonding environments (see §3.4 for the latter).

In most cases, accurately measuring the chlorine CSA is difficult due to the dominant effects of the SOQI on the ^{35}Cl CT patterns. As a result, the uncertainties in the CS tensor parameters (*i.e.*, δ_{iso}, Ω, and κ) and Euler angles, which describe the relative orientations of the different tensors, are often high. This means that unlike the ^{35}Cl EFG tensors, we cannot reliably identify simple correlations between the chlorine CS tensor parameters and the local chloride ion environments.[92] Nonetheless, inclusion of chlorine CS tensor parameters in the simulations aids in differentiating the powder patterns of the different solid forms.

Phenothiazine APIs. The ^{35}Cl SSNMR spectra of the APIs are similar, each displaying a single CT pattern of similar breadths and a relatively low η_Q value (Fig. 1). This similarity is expected based on the crystal structures of these APIs, as all three feature a single chloride ion with a single short H···Cl$^-$ contact of similar lengths (*i.e.*, *ca.* 2.0 Å). Despite the similar chloride ion environments, it is easy to differentiate these APIs based on the ^{35}Cl SSNMR spectra. Of these three APIs, **Ptz** stands out as having the broadest ^{35}Cl spectrum, which is due to the H···Cl$^-$ distance being shorter in **Ptz** than

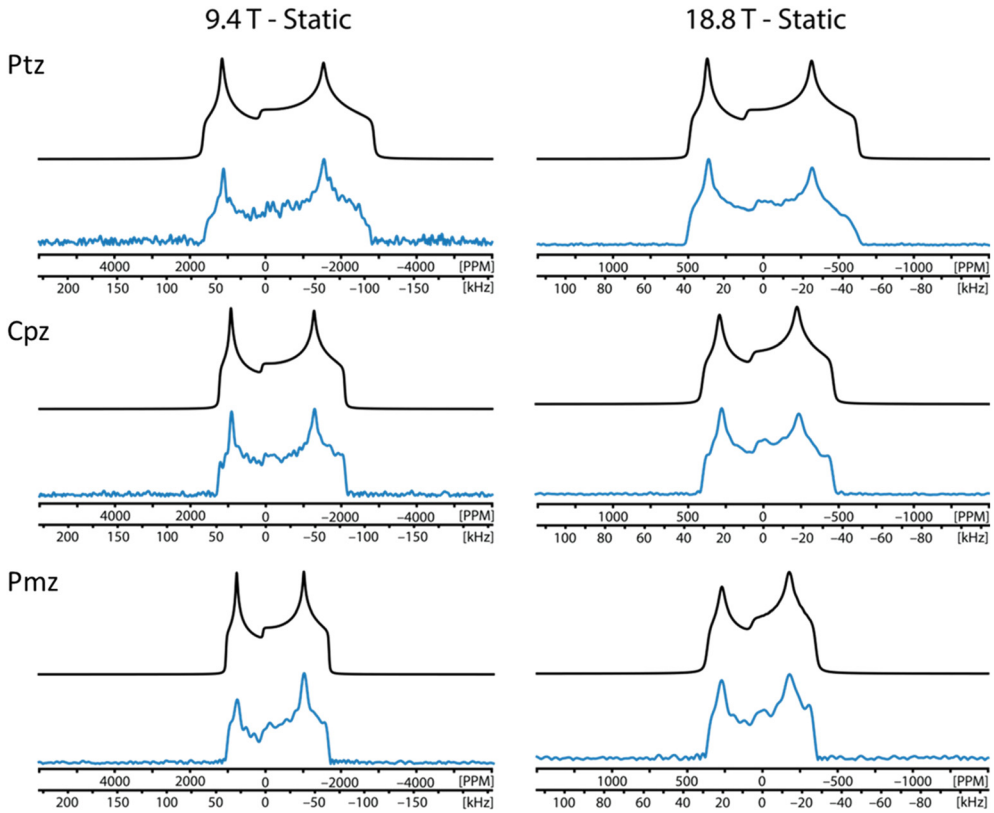

Fig. 1 ^{35}Cl SSNMR spectra of **Ptz**, **Cpz**, and **Pmz** acquired under static conditions at 18.8 T and 9.4 T (blue) and corresponding simulated spectra (black).

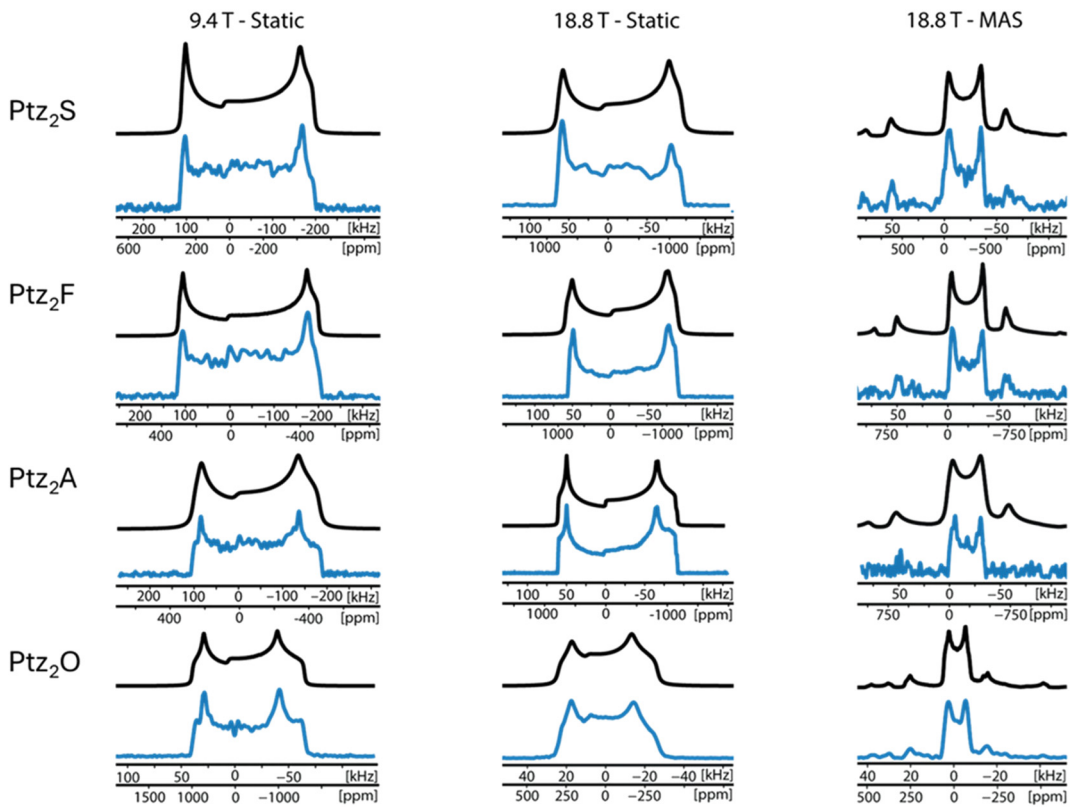

Fig. 2 ^{35}Cl SSNMR spectra and simulations of several **Ptz** cocrystals acquired under static conditions at 9.4 T and static and MAS conditions at 18.8 T.

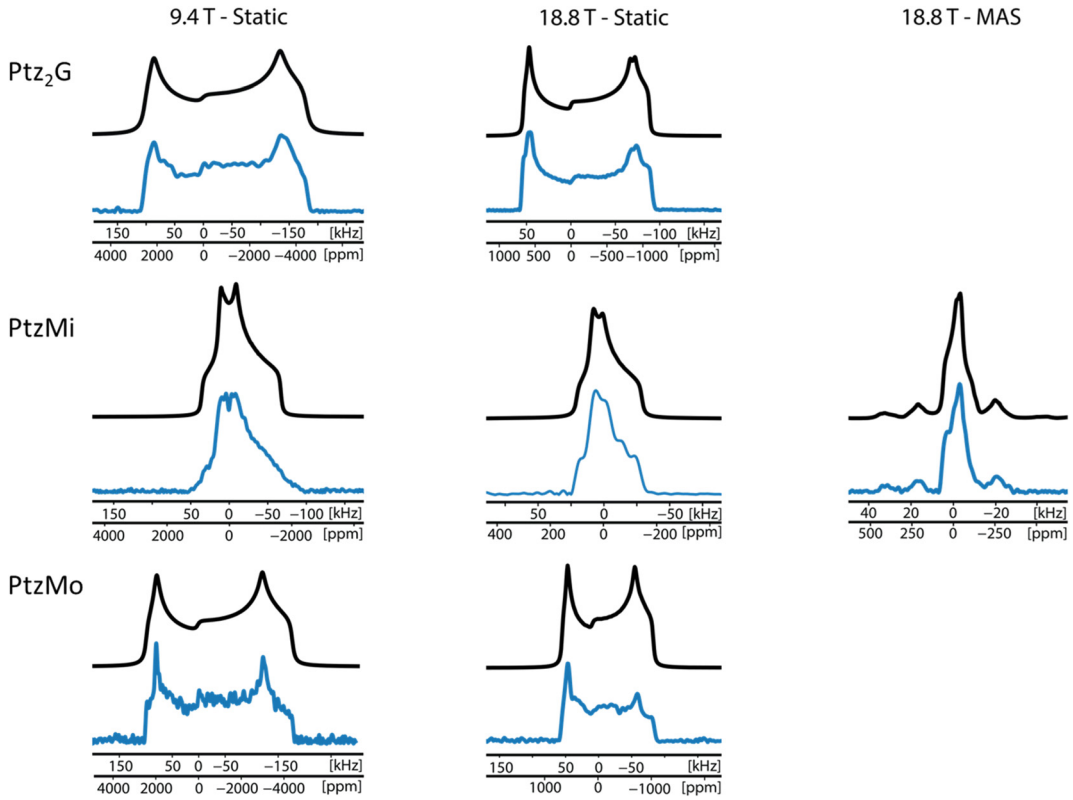

Fig. 3 ^{35}Cl SSNMR spectra and simulations of novel **Ptz** cocrystals acquired under static conditions at 9.4 T and static and MAS conditions at 18.8 T.

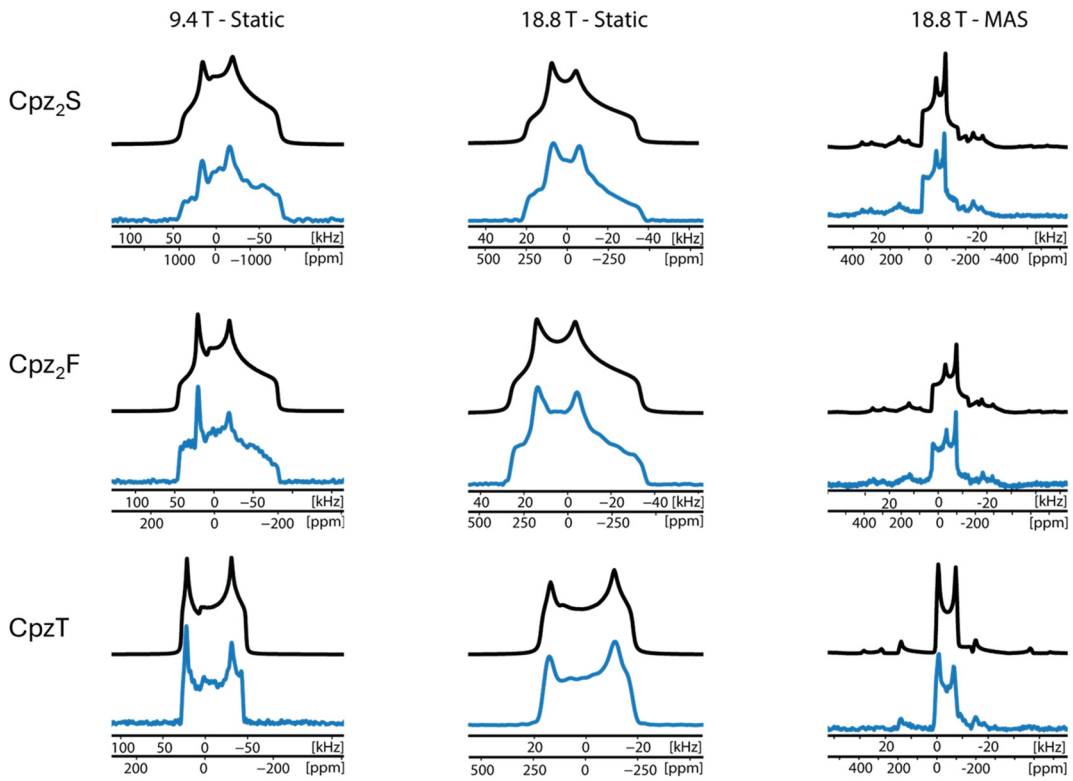

Fig. 4 ^{35}Cl SSNMR spectra and simulations of novel **Cpz** cocrystals acquired under static conditions at 9.4 T and static and MAS conditions at 18.8 T.

in **Cpz** or **Pmz** (Table 4). **Pmz** and **Cpz** have very similar patterns, but **Cpz** is slightly broader. However, they are more easily differentiated by their δ_{iso} (41 and 60 ppm for **Cpz** and **Pmz** respectively). In the spectra of **Cpz**, there is no indication of a second powder pattern corresponding to the covalently bonded chlorine atom; this absence is due to the high C_Q values of covalently bonded chlorine atoms (C_Q is often greater than 60 MHz) resulting in an extremely broad pattern that is difficult to acquire.

Known Ptz cocrystals. All ^{35}Cl SSNMR spectra of the known **Ptz** cocrystals feature a single CT pattern corresponding to single distinct chloride site (Fig. 2). At 18.8 T, the CT patterns are dominated by the SOQI with little trace of CSA effects, having breadths ranging from 50 to 160 kHz. In general, these spectra can be obtained quickly, with prefatory spectra taking only minutes and high-quality spectra usually taking from 2 to 6 hours. None of the ^{35}Cl spectra reveal the presence of unreacted **Ptz**, suggesting that the LAG reactions are quantitative.

The C_Q values of **Ptz$_2$A**, **Ptz$_2$F**, and **Ptz$_2$S** are large in comparison to that of **Ptz** and are at the upper end of those typically observed for chloride ions (*i.e.*, approaching 9–10 MHz), suggesting low spherical symmetries in the surrounding electron density. The range of η_Q values is from 0.05 to 0.25, indicating EFG tensors with high degrees of axial symmetry. Such quadrupolar parameters for chloride ions are usually indicative of hydrogen bonding arrangements featuring two short H$\cdots$Cl$^-$ contacts (*i.e.*, r(H$\cdots$Cl$^-$) $\lesssim$ 2.2 Å) with an almost linear H$\cdots$Cl$^-\cdots$H arrangement (*i.e.*, $\angle$(H$\cdots$Cl$^-\cdots$H) $\approx$ 180°, see §3.4).[42,93,94] Due to the large C_Q values, accurate CS tensor parameters are difficult to obtain, even with data at 18.8 T. In this series, **Ptz$_2$O** is the exception, having a C_Q smaller than that of **Ptz** (*i.e.*, 5.07 and 6.49 MHz, respectively), and a span Ω = 85 ppm. **Ptz$_2$F** and **Ptz$_2$S** have very similar C_Q and η_Q parameters, which is expected because these cocrystals are isostructural; hence, these cocrystals are most easily differentiated in these spectra by their distinct δ_{iso} values (14 and 44 ppm, respectively). Although these cocrystals are isostructural, subtle differences in hydrogen bond lengths influence the local electronic structure, resulting in distinct ^{35}Cl chemical shifts.

Novel Ptz cocrystals. Crystal structures have not been determined for any of the novel **Ptz** cocrystals reported herein; however, comparison of their ^{35}Cl SSNMR spectra (Fig. 3) to those of the known **Ptz** cocrystals lends insight into their structures and aids in future NMR crystallographic analysis. For example, the ^{35}Cl SSNMR spectra of **PtzMo** and **Ptz$_2$G** have large C_Q and small η_Q values, which are suggestive of Cl$^-$ hydrogen bonding arrangements similar to those of **Ptz$_2$A**, **Ptz$_2$F**, and **Ptz$_2$S**. However, in this series, the exception is **PtzMi**, which has the smallest C_Q and largest η_Q of any HCl salt reported herein. There are several HCl APIs with similar C_Q and η_Q values to that of **PtzMi**, most notably yohimbine HCl and procainamide HCl, suggesting that the former may have a similar chloride ion environment. In both of the latter, there are two short contacts $\lesssim$ 2.2 Å, with V_{33} oriented approximately in the direction of the shorter contact.[41,92] **Ptz$_2$G** represents a unique case herein, in that peak doubling is clearly observable in its ^{1}H-^{13}C CP/MAS NMR spectra, which likely indicates either a Z' = 2 unit cell or some degree of disorder. Unfortunately, this cannot be confirmed with absolute certainty *via* the static ^{35}Cl SSNMR spectra, since it is possible to obtain a similar powder pattern using (i) a two-site fit featuring slightly different quadrupolar and chemical shift parameters or (ii) a one-site fit featuring a Ω = 100 ppm, κ = 0.7, and β = 15° (Fig. S10†). Nonetheless, the ^{13}C SSNMR data is convincing in this respect, and may aid in future attempts at NMRX-driven crystal structure prediction. We are continuing to grow single crystals and acquire high quality PXRD data, in the hope of eventually determining these structures *via* NMR-assisted SCXRD or a combination of NMRX and Rietveld refinements.[44,95–98]

Novel Cpz cocrystals. Three novel cocrystals of **Cpz** were also analyzed by ^{35}Cl SSNMR (Fig. 4). The ^{35}Cl CT patterns of **Cpz$_2$S** and **Cpz$_2$F** are similar to each other but reveal values of C_Q that are significantly lower than those of **Ptz$_2$S** and **Ptz$_2$F**, as well as higher values of η_Q, which indicate non-axially symmetric EFG tensors. As with their **Ptz** analogs, the ^{35}Cl CT patterns of **Cpz$_2$S** and **Cpz$_2$F** are most readily differentiated by their disparate values of δ_{iso} (38 and 42 ppm, respectively). The similarity of the ^{35}Cl CT patterns of **CpzT** and **Cpz** indicate that the chloride ions reside in similar environments (though **CpzT** has a higher degree of spherical symmetry around the chloride ion). As in the case of **Cpz**, there is no indication of a second powder pattern corresponding to the covalently bonded chlorine atoms.

3.4 NMR crystallography using ^{35}Cl EFG tensors

Plane-wave DFT calculations were conducted on structural models based on the crystal structures of the three APIs (**Ptz**, **Pmz**, and **Cpz**), four previously reported cocrystals (**Ptz$_2$F**, **Ptz$_2$S**, **Ptz$_2$A**, and **Ptz$_2$O**), and two novel cocrystals (**Cpz$_2$F** and **Cpz$_2$S**). The structural models were geometry optimized using

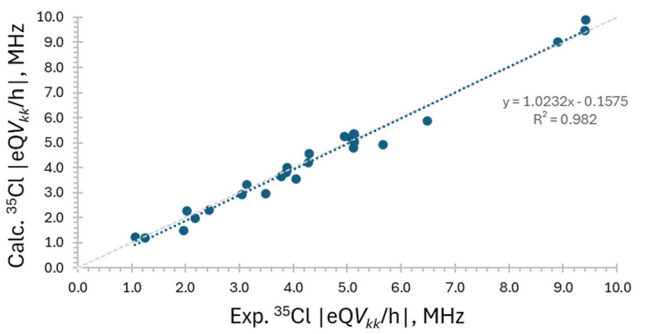

Fig. 5 Relationships between principal components of the ^{35}Cl EFG tensors (*i.e.*, V_{kk}, where k = 1, 2, or 3 – see Table 5 for definitions) that have been measured experimentally and calculated from DFT-D2* geometry-optimized structures. The grey dotted line represents perfect correlation.

Table 6 Comparison of hydrogen bond arrangements to ^{35}Cl EFG parameters

Hydrogen bonding arrangement	Systems	Number of short H···Cl contacts	Range of C_Q values	Range of η_Q values	Respective signs of V_{33} and C_Q	Direction of V_{33}
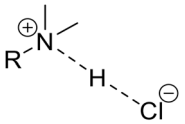	Ptz, Cpz, Pmz	1	~4.5–6.0	~0.0–0.4	+/—	Along/near the hydrogen bond
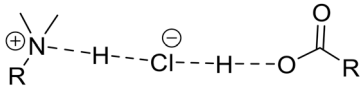	Ptz_2F, Ptz_2S, Ptz_2A, Ptz_2G,[a] PtzMo[a]	2	~8.5–10.0	~0.0–0.2	+/—	Along/near the hydrogen bond (type 1)
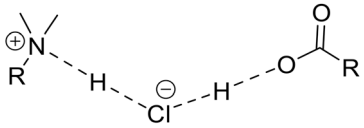	Ptz_2O, Cpz_2S, Cpz_2F, CpzT,[a] PtzMi[a]	2	~4.0–6.0	~0.1–0.7	—/+	Perpendicular to the H···Cl···H plane (type 2)

[a] These materials do not have a known crystal structure.

dispersion-corrected plane-wave DFT calculations (DFT-D2*), which are necessary to obtain low-energy configurations of atoms involved in intermolecular hydrogen-bonding interactions.[45,85] ^{35}Cl EFG and CS tensors were then calculated for the refined structural models (Table 5).

Since there is generally good agreement between experimental and calculated ^{35}Cl EFG tensors (Fig. 5), it is possible to explore their relationships to the structural environments of the chloride ions, which are sensitive to variations in the number and arrangement of short H···Cl$^-$ contacts and the nature of the hydrogen-bonding moieties (Table 6).[32,34,39,41,43,92,94,99] Key interatomic distances and interbond angles obtained from DFT-D2* geometry optimized structures are summarized in Table 4.

The chloride ions of **Ptz**, **Pmz**, and **Cpz** have moderate magnitudes of $|C_Q|$ and low values of η_Q (*i.e.*, the largest component of the EFG tensor, V_{33}, is the distinct component, and V_{11} and V_{22} are similar in magnitude to one another and opposite in sign to V_{33}). Based on the growing database of ^{35}Cl EFG tensor data for cationic organic chloride salts and HCl APIs,[32,34,41,43] these values indicate the presence of a single, short H···Cl$^-$ contact of $\lesssim$ 2.2 Å, with V_{33} oriented along or near its direction. The DFT-D2* refined model structures confirm this, revealing that (i) each has a single RR′R″NH$^+$···Cl$^-$ short contact; (ii) each V_{33} is oriented close to the short contact, with $\angle(V_{33}\cdots Cl^-\cdots H)$ ranging from *ca.* 5° to 11°; (iii) the sign of C_Q is calculated to be negative in all cases (the sign cannot be determined from the experimental ^{35}Cl NMR spectra, but is useful in structural interpretation), which is a result of the negative quadrupole moment, meaning that if $V_{33} > 0$ then $C_Q < 0$; and (iv) the magnitude of $|C_Q|$ would normally be expected to increase with decreasing contact length in the order **Ptz** > **Cpz** > **Pmz** – although **Ptz** has the shortest contact and largest $|C_Q|$, a clear relationship is not discerned for **Cpz** and **Pmz** due to variations in $\angle(V_{33}\cdots Cl^-\cdots H)$ (Fig. S11†).

The **Ptz** cocrystals with known structures are now considered. **Ptz_2F**, **Ptz_2S**, and **Ptz_2A** have large magnitudes of $|C_Q|$ and low values of η_Q. This indicates two short H···Cl$^-$ contacts (*i.e.*, r(H···Cl$^-$) $\lesssim$ 2.2 Å) with $\angle$(H···Cl$^-$···H) approaching 180°, with V_{33} oriented along or near these vectors (Fig. S12†).[100–103] This is borne out by the DFT-D2* calculations, which predict two short H···Cl$^-$ contacts in each system (RR′R″NH$^+$···Cl$^-$ and COOH···Cl$^-$), with the functional groups sitting approximately on opposite sides of the chloride ion (as indicated by the H···Cl$^-$···H angles, which range from *ca.* 153° to 156°), and ^{35}Cl EFG tensors of high axial symmetry with V_{33} (that are positive in sign) oriented near the H···Cl$^-$ contacts.[104]

Ptz_2O stands out in this series, with values of C_Q = 5.07 MHz and η_Q = 0.20, akin to those of the APIs with single short H···Cl$^-$ contacts. Examination of the DFT-D2* structure confirms the presence of R′R$_2$NH$^+$···Cl$^-$ and COOH···Cl$^-$ short contacts, but in an arrangement such that the H···Cl$^-$···H angle is 99.8° (*i.e.*, the moieties are not on opposite sides of the chloride ion). In this instance, V_{33} is not oriented near the short contacts, but rather, approximately perpendicular to the H···Cl$^-$···H plane (Fig. S12†). Furthermore, V_{11} and V_{22}, which reside in the H···Cl$^-$···H plane, are similar in magnitude and positive (V_{33} is negative, unlike the previous systems), consistent with observations for many other systems.[39,42,88,92,94,105,106]

Finally, **Cpz_2F** and **Cpz_2S** feature moderate $|C_Q|$ values and larger η_Q values (the latter indicate EFG tensors of non-axial symmetry, with V_{11} as the distinct component) (Fig. S13†). As in the case of **Ptz_2O**, the ^{35}Cl EFG tensors are oriented such that V_{33} (negative values) are approximately perpendicular to the H···Cl$^-$···H planes (V_{11} and V_{22} are positive and approximately in the planes). Unlike **Ptz_2O**, the RR′R″NH$^+$···Cl$^-$ and COOH···Cl$^-$ contacts have different lengths, with V_{22} aligned nearer to the longer RR′R″NH$^+$···Cl$^-$ contact.

These insights lead to four simple relationships that can be used to make preliminary predictions about the chloride ion environments in cocrystals without known crystal structures and allow us to classify the systems described in this work into one of three possible geometric arrangements

(Table 6). **Ptz_2G** and **PtzMo** have large values of C_Q (>8.8 MHz) and small η_Q values (<0.16), suggesting Cl^- ion environments similar to those of **Ptz_2F**, **Ptz_2S**, and **Ptz_2A**, with two short contacts ($RR'R''NH^+\cdots Cl^-$ and $COOH\cdots Cl^-$) sitting on opposite sides of the chloride ion with an ∠(H···Cl···H) approaching 180°. **CpzT** has an intermediate value of C_Q (4.41 MHz) and small η_Q value (0.04), similar to **Ptz_2O**, which features two short contacts ($RR'R''NH^+\cdots Cl^-$ and $COOH\cdots Cl^-$) with moieties not on opposite sides of the chloride ion and V_{33} orientated *ca.* 90° to the plane of these contacts. **PtzMi** and **PtzMo** are interesting cases, since both have a 1 : 1 ratio of API : coformer, possibly suggesting dimeric structures.[107–109] However, the quadrupolar parameters of **PtzMo** are similar to those of **Ptz_2F**, **Ptz_2S**, **Ptz_2G** and **Ptz_2A**, suggesting an analogous "near-linear" H···Cl···H configuration, whereas for **PtzMi**, its distinct values of C_Q = 4.42 MHz and η_Q = 0.62 suggests an arrangement of contacts similar to **Cpz_2F** and **Cpz_2S** (*i.e.*, ∠(H···Cl^-···H) of *ca.* 90–100°, with longer $RR'R''NH^+\cdots Cl^-$ and shorter $COOH\cdots Cl^-$ contacts). In the case of **PtzMo**, we propose four possible arrangements based on crystal structures of pure malonic acid and several concomitant solid forms (in a 1 : 1 stoichiometric ratio) found in the literature (Scheme S2†).[110–113] Of these, we consider arrangement B the most plausible, as it would likely result in the densest crystal packing.

Without geometry-optimized structures and corresponding ^{35}Cl EFG tensors that can be obtained from DFT calculations, we are currently limited to these simple structural interpretations. However, these experimental data, along with the combined experimental and calculated NMR data from well-characterized systems and high-quality PXRD data for Rietveld refinement, may inform future NMRX solutions of these structures and others. This will be pursued using the data herein along with our separate and continuing efforts on ^{35}Cl SSNMR-based NMRX methods, including quadrupolar-guided NMR crystallography crystal structure prediction (QNMRX-CSP) methods.[3,41,44,51,92]

4. Conclusions

This study has demonstrated: (i) the rapid and quantitative mechanochemical synthesis of eleven ionic HCl cocrystals featuring two cationic APIs, a number of neutral, pharmaceutically acceptable coformers, and chloride ions; (ii) the advantages of mechanochemical methods, including their optimization for efficiency and application for discovering novel cocrystals; (iii) the value of ^{35}Cl SSNMR spectroscopy for the analysis of known **Ptz** cocrystals and elucidation of novel **Ptz** and **Cpz** cocrystal structures; and (iv) the use of plane-wave DFT calculations of ^{35}Cl EFG tensors to investigate their relationships to the complex hydrogen bonding networks of the chloride ions.

This combination of mechanochemical synthesis and subsequent characterization has extended our knowledge in terms of what is possible for synthesizing cocrystals of this largely unexplored class of ionic HCl API cocrystals, which may allow us to rationally choose coformers that will lead to an increased number of novel pharmaceutical cocrystals, and perhaps even achieve novel forms of promazine HCl cocrystals, which have been unsuccessful to date – at this point, we are unclear why this is the case for **Pmz**, since the only difference between the molecular structures of **Cpz** and **Pmz** is a covalently-bound chlorine atom in the former. To determine and refine crystal structures for novel cocrystals using SSNMR of quadrupolar nuclides, we have two promising options going forward: (i) our new QNMRX-CSP protocol and (ii) NMR-guided Rietveld refinement.[50,51,114–116]

Data availability

The data supporting this article have been included as part of the ESI.† Crystallographic data have been deposited at the CCDC under 2425375 and 2425 376.

Conflicts of interest

There are no conflicts to declare.

Acknowledgements

The authors thank the Florida State University and the National High Magnetic Field Laboratory for funding this research. The National High Magnetic Field Laboratory was supported by the National Science Foundation through NSF/DMR-1644779, DMR-2128556 and the State of Florida. The authors also thank the Natural Sciences and Engineering Research Council of Canada (NSERC Discovery grants 2016-06642 and 2020-04627 for RWS and JMR, respectively), the Canadian Foundation for Innovation, the Ontario Innovation Trust, the Ontario Research Fund, and the University of Windsor for supporting the initial stages of this project. A portion of this research used resources provided by the X-ray Crystallography Center at the FSU Department of Chemistry and Biochemistry. The authors also acknowledge use of the SSNMR and SCXRD facilities at the University of Windsor, supported by the Canadian Foundation for Innovation, Ontario Innovation Trust, and the University of Windsor.

References

1 M. Geppi, G. Mollica, S. Borsacchi and C. A. Veracini, Solid-State NMR Studies of Pharmaceutical Systems, *Appl. Spectrosc. Rev.*, 2008, **43**(3), 202–302, DOI: **10.1080/05704920801944338**.

2 N. K. Duggirala, M. L. Perry, Ö. Almarsson and M. J. Zaworotko, Pharmaceutical Cocrystals: Along the Path to Improved Medicines, *Chem. Commun.*, 2016, **52**(4), 640–655, DOI: **10.1039/C5CC08216A**.

3 H. Hamaed, J. M. Pawlowski, B. F. T. T. Cooper, R. Fu, S. H. Eichhorn and R. W. Schurko, Application of Solid-State 35Cl NMR to the Structural Characterization of

Hydrochloride Pharmaceuticals and Their Polymorphs, *J. Am. Chem. Soc.*, 2008, **130**(33), 11056–11065, DOI: **10.1021/ja802486q**.

4 G. S. Paulekuhn, J. B. Dressman and C. Saal, Trends in Active Pharmaceutical Ingredient Salt Selection Based on Analysis of the Orange Book Database, *J. Med. Chem.*, 2007, **50**(26), 6665–6672, DOI: **10.1021/JM701032Y**.

5 S. Aitipamula, R. Banerjee, A. K. Bansal, K. Biradha, M. L. Cheney, A. R. Choudhury, G. R. Desiraju, A. G. Dikundwar and M. J. Zaworotko, Salts, and Cocrystals: What's in a Name?, *Cryst. Growth Des.*, 2012, **12**(5), 2147–2152, DOI: **10.1021/CG3002948**.

6 S. L. Childs, L. J. Chyall, J. T. Dunlap, V. N. Smolenskaya, B. C. Stahly and G. P. Stahly, Crystal Engineering Approach To Forming Cocrystals of Amine Hydrochlorides with Organic Acids. Molecular Complexes of Fluoxetine Hydrochloride with Benzoic, Succinic, and Fumaric Acids, *J. Am. Chem. Soc.*, 2004, **126**(41), 13335–13342, DOI: **10.1021/ja048114o**.

7 S. Datta and D. J. W. Grant, Crystal Structures of Drugs: Advances in Determination, Prediction and Engineering, *Nat. Rev. Drug Discovery*, 2004, **3**(1), 42–57, DOI: **10.1038/nrd1280**.

8 A. M. Healy, Z. A. Worku, D. Kumar and A. M. Madi, Pharmaceutical Solvates, Hydrates and Amorphous Forms: A Special Emphasis on Cocrystals, *Adv. Drug Delivery Rev.*, 2017, **117**, 25–46, DOI: **10.1016/J.ADDR.2017.03.002**.

9 E. Pindelska, A. Sokal and W. Kolodziejski, Pharmaceutical Cocrystals, Salts and Polymorphs: Advanced Characterization Techniques, *Adv. Drug Delivery Rev.*, 2017, **117**, 111–146, DOI: **10.1016/J.ADDR.2017.09.014**.

10 G. Borodi, A. Turza, O. Onija and A. Bende, Succinic, Fumaric, Adipic and Oxalic Acid Cocrystals of Promethazine Hydrochloride, *Acta Crystallogr., Sect. C: Struct. Chem.*, 2019, **75**(2), 107–119, DOI: **10.1107/S2053229618017904**.

11 A. Olejniczak, K. Krukle-Berziņa and A. Katrusiak, Pressure-Stabilized Solvates of Xylazine Hydrochloride, *Cryst. Growth Des.*, 2016, **16**(7), 3756–3762, DOI: **10.1021/ACS.CGD.6B00264**.

12 A. Saha, A. A. Ahangar, A. A. Dar, S. Thirunahari and J. V. Parambil, Pharmaceutical Cocrystals: A Perspective on Development and Scale-up of Solution Cocrystallization, *Cryst. Growth Des.*, 2023, **23**(11), 7558–7581, DOI: **10.1021/acs.cgd.2c01553**.

13 N. Pawar, A. Saha, N. Nandan and J. V. Parambil, Solution Cocrystallization: A Scalable Approach for Cocrystal Production, *Crystals*, 2021, **11**(3), 303, DOI: **10.3390/CRYST11030303**.

14 S. N. Madanayake, A. Manipura, R. Thakuria and N. M. Adassooriya, Opportunities and Challenges in Mechanochemical Cocrystallization toward Scaled-Up Pharmaceutical Manufacturing, *Org. Process Res. Dev.*, 2023, **27**(3), 409–422, DOI: **10.1021/acs.oprd.2c00314**.

15 M. S. Hossain Mithu, S. Economidou, V. Trivedi, S. Bhatt and D. Douroumis, Advanced Methodologies for Pharmaceutical Salt Synthesis, *Cryst. Growth Des.*, 2021, **21**(2), 1358–1374, DOI: **10.1021/acs.cgd.0c01427**.

16 A. R. Buist, A. R. Kennedy and C. Manzie, Four Salt Phases of Theophylline, *Acta Crystallogr., Sect. C:Struct. Chem.*, 2014, **70**(2), 220–224, DOI: **10.1107/S2053229614000825**.

17 M. R. J. Elsegood, D. A. Hussain and N. M. Sanchez-Ballester, Redetermination of Picolinic Acid Hydro-Chloride at 150 K, *Acta Crystallogr., Sect. E: Struct. Rep. Online*, 2007, **63**(10), o4044–o4044, DOI: **10.1107/S1600536807044030**.

18 H. Ferjani, H. Chebbi, A. Guesmi, O. S. Alruqi and S. A. Al-Hussain, Two-Dimensional Hydrogen-Bonded Crystal Structure, Hirshfeld Surface Analysis and Morphology Prediction of a New Polymorph of 1H-Nicotineamidium Chloride Salt, *Crystals*, 2019, **9**(11), 571, DOI: **10.3390/CRYST9110571**.

19 D. E. Crawford, C. K. G. Miskimmin, A. B. Albadarin, G. Walker and S. L. James, Organic Synthesis by Twin Screw Extrusion (TSE): Continuous, Scalable and Solvent-Free, *Green Chem.*, 2017, **19**(6), 1507–1518, DOI: **10.1039/C6GC03413F**.

20 D. J. Berry, C. C. Seaton, W. Clegg, R. W. Harrington, S. J. Coles, P. N. Horton, M. B. Hursthouse, R. Storey and N. Blagden, Applying Hot-Stage Microscopy to Co-Crystal Screening: A Study of Nicotinamide with Seven Active Pharmaceutical Ingredients, *Cryst. Growth Des.*, 2008, **8**(5), 1697–1712, DOI: **10.1021/cg800035w**.

21 T. Stolar and K. Užarević, Mechanochemistry: An Efficient and Versatile Toolbox for Synthesis, Transformation, and Functionalization of Porous Metal–Organic Frameworks, *CrystEngComm*, 2020, **22**(27), 4511–4525, DOI: **10.1039/D0CE00091D**.

22 A. Bodach, A. Portet, F. Winkelmann, B. Herrmann, F. Gallou, E. Ponnusamy, D. Virieux, E. Colacino and M. Felderhoff, Scalability of Pharmaceutical Co-Crystal Formation by Mechanochemistry in Batch, *ChemSusChem*, 2024, **17**(6), e202301220, DOI: **10.1002/CSSC.202301220**.

23 K. Trzeciak, M. K. Dudek and M. J. Potrzebowski, Mechanochemical Transformations of Pharmaceutical Cocrystals: Polymorphs and Coformer Exchange, *Chem. – Eur. J.*, 2024, **30**(71), e202402683, DOI: **10.1002/CHEM.202402683**.

24 J.-H. Schöbel, F. Winkelmann, J. Bicker and M. Felderhoff, Mechanochemical Kilogram-Scale Synthesis of Rac - Ibuprofen:Nicotinamide Co-Crystals Using a Drum Mill, *RSC Mechanochem.*, 2025, **2**, 224–229, DOI: **10.1039/D4MR00096J**.

25 D. Šilić, B. Cetina-Čižmek, M. Antonijevic and D. Douroumis, One-Step Synthesis of a Drug-Drug Cocrystal Hydrate Using Hot Melt Extrusion, *Cryst. Growth Des.*, 2024, **24**(19), 8044–8055, DOI: **10.1021/acs.cgd.4c00974**.

26 T. Friščić, C. Mottillo and H. M. Titi, Mechanochemistry for Synthesis, *Angew. Chem., Int. Ed.*, 2019, 1018–1029, DOI: **10.1002/anie.201906755**.

27 L. S. Germann, M. Arhangelskis, M. Etter, R. E. Dinnebier and T. Friščić, Challenging the Ostwald Rule of Stages in Mechanochemical Cocrystallisation, *Chem. Sci.*, 2020, **11**, 10092–10100, DOI: **10.1039/d0sc03629c**.

28 F. Fischer, D. Lubjuhn, S. Greiser, K. Rademann and F. Emmerling, Supply and Demand in the Ball Mill: Competitive Cocrystal Reactions, *Cryst. Growth Des.*, 2016, **16**(10), 5843–5851, DOI: **10.1021/acs.cgd.6b00928**.

29 D. Margetić and V. Štrukil, *Practical Considerations in Mechanochemical Organic Synthesis*, 2016, DOI: **10.1016/b978-0-12-802184-2.00001-7**.

30 T. Friić, S. L. Childs, S. A. A. Rizvi and W. Jones, The Role of Solvent in Mechanochemical and Sonochemical Cocrystal Formation: A Solubility-Based Approach for Predicting Cocrystallisation Outcome, *CrystEngComm*, 2009, **11**(3), 418–426, DOI: **10.1039/B815174A**.

31 D. Braga, S. L. Giaffreda, F. Grepioni, A. Pettersen, L. Maini, M. Curzi and M. Polito, Mechanochemical Preparation of Molecular and Supramolecular Organometallic Materials and Coordination Networks, *Dalton Trans.*, 2006(10), 1249–1263, DOI: **10.1039/B516165G**.

32 H. Hamaed, J. M. Pawlowski, B. F. T. Cooper, R. Fu, S. H. Eichhorn and R. W. Schurko, Application of Solid-State 35 Cl NMR to the Structural Characterization of Hydrochloride Pharmaceuticals and Their Polymorphs, *J. Am. Chem. Soc.*, 2008, **130**(33), 11056–11065, DOI: **10.1021/ja802486q**.

33 D. A. Hirsh, A. J. Rossini, L. Emsley and R. W. Schurko, 35Cl Dynamic Nuclear Polarization Solid-State NMR of Active Pharmaceutical Ingredients, *Phys. Chem. Chem. Phys.*, 2016, **18**(37), 25893–25904, DOI: **10.1039/c6cp04353d**.

34 D. L. Bryce and G. D. Sward, Chlorine-35/37 NMR Spectroscopy of Solid Amino Acid Hydrochlorides: Refinement of Hydrogen-Bonded Proton Positions Using Experiment and Theory, *J. Phys. Chem. B*, 2006, **110**(51), 26461–26470, DOI: **10.1021/jp065878c**.

35 P. M. J. Szell and D. L. Bryce, Cl Solid-State NMR and Computational Study of Chlorine Halogen Bond Donors in Single-Component Crystalline Chloronitriles, *J. Phys. Chem. C*, 2016, **120**(20), 11121–11130, DOI: **10.1021/acs.jpcc.6b02806**.

36 J. Struppe, C. M. Quinn, S. Sarkar, A. M. Gronenborn and T. Polenova, Ultrafast 1 H MAS NMR Crystallography for Natural Abundance Pharmaceutical Compounds, *Mol. Pharmaceutics*, 2020, **17**(2), acs.molpharmaceut.9b01157, DOI: **10.1021/acs.molpharmaceut.9b01157**.

37 F. G. Vogt, G. R. Williams, M. Strohmeier, M. N. Johnson and R. C. B. Copley, Solid-State NMR Analysis of a Complex Crystalline Phase of Ronacaleret Hydrochloride, *J. Phys. Chem. B*, 2014, **118**(34), 10266–10284, DOI: **10.1021/jp505061j**.

38 M. K. Pandey, H. Kato, Y. Ishii and Y. Nishiyama, Two-Dimensional Proton-Detected 35Cl/1H Correlation Solid-State NMR Experiment under Fast Magic Angle Sample Spinning: Application to Pharmaceutical Compounds, *Phys. Chem. Chem. Phys.*, 2016, **18**(8), 6209–6216, DOI: **10.1039/C5CP06042G**.

39 L. M. Abdulla, A. A. Peach, S. T. Holmes, Z. T. Dowdell, L. K. Watanabe, E. M. Iacobelli, D. A. Hirsh, J. M. Rawson and R. W. Schurko, Synthesis and Characterization of Xylazine Hydrochloride Polymorphs, Hydrates, and Cocrystals: A 35Cl Solid-State NMR and DFT Study, *Cryst. Growth Des.*, 2023, **23**(5), 3412–3426, DOI: **10.1021/acs.cgd.2c01539**.

40 A. J. Stirk, S. T. Holmes, F. E. S. Souza, I. Hung, Z. Gan, J. F. Britten, A. W. Rey and R. W. Schurko, An Unusual Ionic Cocrystal of Ponatinib Hydrochloride: Characterization by Single-Crystal X-Ray Diffraction and Ultra-High Field NMR Spectroscopy, *CrystEngComm*, 2024, **26**(9), 1219–1233, DOI: **10.1039/D3CE01062G**.

41 M. Hildebrand, H. Hamaed, A. M. Namespetra, J. M. Donohue, R. Fu, I. Hung, Z. Gan and R. W. Schurko, 35 Cl Solid-State NMR of HCl Salts of Active Pharmaceutical Ingredients: Structural Prediction, Spectral Fingerprinting and Polymorph Recognition, *CrystEngComm*, 2014, **16**(31), 7334–7356, DOI: **10.1039/C4CE00544A**.

42 A. A. Peach, D. A. Hirsh, S. T. Holmes and R. W. Schurko, Mechanochemical Syntheses and 35 Cl Solid-State NMR Characterization of Fluoxetine HCl Cocrystals, *CrystEngComm*, 2018, **20**(20), 2780–2792, DOI: **10.1039/C8CE00378E**.

43 A. M. Namespetra, D. A. Hirsh, M. P. Hildebrand, A. R. Sandre, H. Hamaed, J. M. Rawson and R. W. Schurko, 35Cl Solid-State NMR Spectroscopy of HCl Pharmaceuticals and Their Polymorphs in Bulk and Dosage Forms, *CrystEngComm*, 2016, **18**(33), 6213–6232, DOI: **10.1039/c6ce01069e**.

44 C. S. Vojvodin, S. T. Holmes, L. K. Watanabe, J. M. Rawson and R. W. Schurko, Multi-Component Crystals Containing Urea: Mechanochemical Synthesis and Characterization by 35 Cl Solid-State NMR Spectroscopy and DFT Calculations, *CrystEngComm*, 2022, **24**(14), 2626–2641, DOI: **10.1039/D1CE01610E**.

45 S. T. Holmes, C. S. Vojvodin and R. W. Schurko, Dispersion-Corrected DFT Methods for Applications in Nuclear Magnetic Resonance Crystallography, *J. Phys. Chem. A*, 2020, **124**(49), 10312–10323, DOI: **10.1021/acs.jpca.0c06372**.

46 S. T. Holmes and R. W. Schurko, Refining Crystal Structures with Quadrupolar NMR and Dispersion-Corrected Density Functional Theory, *J. Phys. Chem. C*, 2018, **122**(3), 1809–1820, DOI: **10.1021/acs.jpcc.7b12314**.

47 D. L. Bryce, NMR Crystallography: Structure and Properties of Materials from Solid-State Nuclear Magnetic Resonance Observables, *IUCrJ*, 2017, **4**(4), 350–359, DOI: **10.1107/S2052252517006042**.

48 P. Hodgkinson, NMR Crystallography of Molecular Organics, *Prog. Nucl. Magn. Reson. Spectrosc.*, 2020, **118–119**, 10–53, DOI: **10.1016/J.PNMRS.2020.03.001**.

49 F. Taulelle, *Fundamental Principles of NMR Crystallography*, John Wiley & Sons, Ltd, Chichester, UK, 2009, DOI: **10.1002/9780470034590.emrstm1003**.

50 A. A. Peach, C. H. Fleischer, K. Levin, S. T. Holmes, J. E. Sanchez and R. W. Schurko, Quadrupolar NMR Crystallography Guided Crystal Structure Prediction (QNMRX-CSP), *CrystEngComm*, 2024, **26**(35), 4782–4803, DOI: **10.1039/D3CE01306E**.

51 C. H. Fleischer, S. T. Holmes, K. Levin, S. L. Veinberg and R. W. Schurko, Characterization of Ephedrine HCl and

Pseudoephedrine HCl Using Quadrupolar NMR Crystallography Guided Crystal Structure Prediction, *Faraday Discuss.*, 2025, **255**(0), 88–118, DOI: **10.1039/D4FD00089G**.

52 D. Feil, M. H. Linck and J. J. H. McDowell, Preliminary X-Ray Data on Phenothiazine and Certain of Its Derivatives, *Nature*, 1965, **207**(4994), 285–286, DOI: **10.1038/207285a0**DOI: **10.1038/207285a0**.

53 W. I. F. David, K. Shankland and N. Shankland, Routine Determination of Molecular Crystal Structures from Powder Diffraction Data, *Chem. Commun.*, 1998, 931–932, DOI: **10.1039/A800855H**.

54 C. J. Brown and IUCr., The Crystal Structure of Fumaric Acid, *Acta Crystallogr.*, 1966, **21**(1), 1–5, DOI: **10.1107/S0365110X66002226**.

55 V. R. Thalladi, M. Nüsse and R. Boese, The Melting Point Alternation in α,ω-Alkanedicarboxylic Acids, *J. Am. Chem. Soc.*, 2000, **122**(38), 9227–9236, DOI: **10.1021/JA0011459**.

56 G. Borodi, M. M. Pop, O. Onija and X. Filip, Distinct Disordered Forms of Promethazine Hydrochloride: A Case of Intergrowth of Polymorphic Domains?, *Cryst. Growth Des.*, 2012, **12**(12), 5846–5851, DOI: **10.1021/cg300943b**DOI: **10.1021/cg300943b**.

57 *CrystalDiffract Overview*, **http://crystalmaker.com/crystaldiffract/** (accessed 2022-11-11).

58 *Bruker, SAINT*, Bruker AXS Inc, Bruker AXS Inc., Madison, WI, USA, 2002.

59 *Bruker, SADABS*, Bruker AXS Inc., Madison, WI, USA, 2002.

60 G. M. Sheldrick, IUCr, SHELXT – Integrated Space-Group and Crystal-Structure Determination, *Acta Crystallogr.*, 2015, **71**(1), 3–8, DOI: **10.1107/S2053273314026370**.

61 G. M. Sheldrick, Crystal Structure Refinement with SHELXL, *Acta Crystallogr.*, 2015, **71**(1), 3–8, DOI: **10.1107/S2053229614024218**.

62 O. V. Dolomanov, L. J. Bourhis, R. J. Gildea, J. A. K. Howard and H. Puschmann, OLEX2: A Complete Structure Solution, Refinement and Analysis Program, *J. Appl. Crystallogr.*, 2009, **42**(2), 339–341, DOI: **10.1107/S0021889808042726**.

63 L. A. O'Dell, A. J. Rossini and R. W. Schurko, Acquisition of Ultra-Wideline NMR Spectra from Quadrupolar Nuclei by Frequency Stepped WURST–QCPMG, *Chem. Phys. Lett.*, 2009, **468**(4–6), 330–335, DOI: **10.1016/j.cplett.2008.12.044**.

64 L. A. O'Dell and R. W. Schurko, QCPMG Using Adiabatic Pulses for Faster Acquisition of Ultra-Wideline NMR Spectra, *Chem. Phys. Lett.*, 2008, **464**(1–3), 97–102, DOI: **10.1016/J.CPLETT.2008.08.095**.

65 R. Bhattacharyya and L. Frydman, Quadrupolar Nuclear Magnetic Resonance Spectroscopy in Solids Using Frequency-Swept Echoing Pulses, *J. Chem. Phys.*, 2007, **127**(19), 194503, DOI: **10.1063/1.2793783**.

66 Ē. Kupče and R. Freeman, Adiabatic Pulses for Wideband Inversion and Broadband Decoupling, *J. Magn. Reson., Ser. A*, 1995, **115**(2), 273–276, DOI: **10.1006/JMRA.1995.1179**.

67 F. H. Larsen, H. J. Jakobsen, P. D. Ellis and N. C. Nielsen, QCPMG-MAS NMR of Half-Integer Quadrupolar Nuclei, *J. Magn. Reson.*, 1998, **131**(1), 144–147, DOI: **10.1006/JMRE.1997.1341**.

68 O. B. Peersen, X. Wu, I. Kustanovich and S. O. Smith, Variable-Amplitude Cross-Polarization MAS NMR, *J. Magn. Reson., Ser. A*, 1993, **104**(3), 334–339, DOI: **10.1006/JMRA.1993.1231**.

69 G. Metz, X. Wu and S. O. Smith, Ramped-Amplitude Cross Polarization in Magic-Angle-Spinning NMR, *J. Magn. Reson., Ser. A*, 1994, **110**(2), 219–227, DOI: **10.1006/JMRA.1994.1208**.

70 J. Schaefer and E. O. Stejskal, Carbon-13 Nuclear Magnetic Resonance of Polymers Spinning at the Magic Angle, *J. Am. Chem. Soc.*, 1976, **98**(4), 1031–1032, DOI: **10.1021/JA00420A036**.

71 A. Pines, M. G. Gibby and J. S. Waugh, Proton-Enhanced Nuclear Induction Spectroscopy 13C Chemical Shielding Anisotropy in Some Organic Solids, *Chem. Phys. Lett.*, 1972, **15**(3), 373–376, DOI: **10.1016/0009-2614(72)80191-X**.

72 A. Pines, M. G. Gibby and J. S. Waugh, Proton-enhanced NMR of Dilute Spins in Solids, *J. Chem. Phys.*, 1973, **59**(2), 569–590, DOI: **10.1063/1.1680061**.

73 B. M. Fung, A. K. Khitrin and K. Ermolaev, An Improved Broadband Decoupling Sequence for Liquid Crystals and Solids, *J. Magn. Reson.*, 2000, **142**(1), 97–101, DOI: **10.1006/JMRE.1999.1896**.

74 R. E. Taylor, 13C CP/MAS: Application to Glycine, *Concepts Magn. Reson., Part A*, 2004, **22A**(2), 79–89, DOI: **10.1002/CMR.A.20015**.

75 M. J. Potrzebowski, P. Tekely and Y. Dusausoy, Comment to 13C-NMR Studies of α and γ Polymorphs of Glycine, *Solid State Nucl. Magn. Reson.*, 1998, **11**(3–4), 253–257, DOI: **10.1016/S0926-2040(98)00028-9**.

76 S. G. J. van Meerten, W. M. J. Franssen and A. P. M. Kentgens, SsNake: A Cross-Platform Open-Source NMR Data Processing and Fitting Application, *J. Magn. Reson.*, 2019, **301**, 56–66, DOI: **10.1016/J.JMR.2019.02.006**.

77 K. Eichele *WSolids1 ver. 1.21.7*, **http://anorganik.uni-tuebingen.de/klaus/soft/index.php?p=wsolids1/wsolids1** (accessed 2025-01-12).

78 M. C. Payne, M. P. Teter, D. C. Allan, T. A. Arias and J. D. Joannopoulos, Iterative Minimization Techniques for Ab Initio Total-Energy Calculations: Molecular Dynamics and Conjugate Gradients, *Rev. Mod. Phys.*, 1992, **64**(4), 1045, DOI: **10.1103/RevModPhys.64.1045**.

79 S. J. Clark, M. D. Segall, C. J. Pickard, P. J. Hasnip, M. I. J. Probert, K. Refson and M. C. Payne, First Principles Methods Using CASTEP, *Z. Kristallogr. - Cryst. Mater.*, 2005, **220**(5–6), 567–570, DOI: **10.1524/zkri.220.5.567.65075**.

80 B. Hammer, L. B. Hansen and J. K. Nørskov, Improved Adsorption Energetics within Density-Functional Theory Using Revised Perdew-Burke-Ernzerhof Functionals, *Phys. Rev. B: Condens. Matter Mater. Phys.*, 1999, **59**(11), 7413, DOI: **10.1103/PhysRevB.59.7413**.

81 J. R. Yates, C. J. Pickard and F. Mauri, Calculation of NMR Chemical Shifts for Extended Systems Using Ultrasoft Pseudopotentials, *Phys. Rev. B: Condens. Matter Mater. Phys.*, 2007, **76**(2), 024401, DOI: **10.1103/PhysRevB.76.024401**.

82 B. G. Pfrommer, M. Côté, S. G. Louie and M. L. Cohen, Relaxation of Crystals with the Quasi-Newton Method, *J. Comput. Phys.*, 1997, **131**(1), 233–240, DOI: **10.1006/JCPH.1996.5612**.

83 S. Grimme, Semiempirical GGA-Type Density Functional Constructed with a Long-Range Dispersion Correction, *J. Comput. Chem.*, 2006, **27**(15), 1787–1799, DOI: **10.1002/jcc.20495**.

84 E. R. McNellis, J. Meyer and K. Reuter, Azobenzene at Coinage Metal Surfaces: Role of Dispersive van Der Waals Interactions, *Phys. Rev. B: Condens. Matter Mater. Phys.*, 2009, **80**(20), 205414, DOI: **10.1103/PHYSREVB.80.205414**.

85 S. T. Holmes and R. W. Schurko, Refining Crystal Structures with Quadrupolar NMR and Dispersion-Corrected Density Functional Theory, *J. Phys. Chem. C*, 2018, **122**(3), 1809–1820, DOI: **10.1021/acs.jpcc.7b12314**.

86 S. T. Holmes, R. J. Iuliucci, K. T. Mueller and C. Dybowski, Semi-Empirical Refinements of Crystal Structures Using 17O Quadrupolar-Coupling Tensors, *J. Chem. Phys.*, 2017, **146**(6), 064201, DOI: **10.1063/1.4975170**.

87 S. T. Holmes, C. S. Vojvodin and R. W. Schurko, Dispersion-Corrected DFT Methods for Applications in Nuclear Magnetic Resonance Crystallography, *J. Phys. Chem. A*, 2020, **124**(49), 10312–10323, DOI: **10.1021/acs.jpca.0c06372**.

88 S. T. Holmes, O. G. Engl, M. N. Srnec, J. D. Madura, R. Quiñones, J. K. Harper, R. W. Schurko and R. J. Iuliucci, Chemical Shift Tensors of Cimetidine Form A Modeled with Density Functional Theory Calculations: Implications for NMR Crystallography, *J. Phys. Chem. A*, 2020, **124**(16), 3109–3119, DOI: **10.1021/acs.jpca.0c00421**.

89 C. J. Pickard and F. Mauri, All-Electron Magnetic Response with Pseudopotentials: NMR Chemical Shifts, *Phys. Rev. B: Condens. Matter Mater. Phys.*, 2001, **63**(24), 245101, DOI: **10.1103/PhysRevB.63.245101**.

90 S. Adiga, D. Aebi and D. L. Bryce, EFGShield — A Program for Parsing and Summarizing the Results of Electric Field Gradient and Nuclear Magnetic Shielding Tensor Calculations, *Can. J. Chem.*, 2011, **85**(7–8), 496–505, DOI: **10.1139/V07-069**.

91 T. Friščić, New Opportunities for Materials Synthesis Using Mechanochemistry, *J. Mater. Chem.*, 2010, **20**(36), 7599–7605, DOI: **10.1039/C0JM00872A**.

92 S. T. Holmes, J. M. Hook and R. W. Schurko, Nutraceuticals in Bulk and Dosage Forms: Analysis by 35Cl and 14N Solid-State NMR and DFT Calculations, *Mol. Pharmaceutics*, 2022, **19**(2), 440–455, DOI: **10.1021/ACS.MOLPHARMACEUT.1C00708**.

93 A. A. Peach, S. T. Holmes, L. R. MacGillivray and R. W. Schurko, The Formation and Stability of Fluoxetine HCl Cocrystals Investigated by Multicomponent Milling, *CrystEngComm*, 2023, **25**(2), 213–224, DOI: **10.1039/D2CE01341J**.

94 A. A. Peach, D. A. Hirsh, S. T. Holmes and R. W. Schurko, Mechanochemical Syntheses and 35 Cl Solid-State NMR Characterization of Fluoxetine HCl Cocrystals, *CrystEngComm*, 2018, **20**(20), 2780–2792, DOI: **10.1039/C8CE00378E**.

95 O. Al Rahal, P. Andrew Williams, C. E. Hughes, B. M. Kariuki and K. D. M. Harris, Structure Determination of Multicomponent Crystalline Phases of (S)-Ibuprofen and L-Proline from Powder X-Ray Diffraction Data, Augmented by Complementary Experimental and Computational Techniques Published as Part of a Crystal Growth and Design Virtual Special Issue on The Rietveld Refinement Method: Half of a Century Anniversary, Cite This, *Cryst. Growth Des.*, 2021, **21**(4), 2498–2507, DOI: **10.1021/acs.cgd.1c00160**.

96 A. A. Peach, C. H. Fleischer, K. Levin, S. T. Holmes, J. E. Sanchez and R. W. Schurko, Quadrupolar NMR Crystallography Guided Crystal Structure Prediction (QNMRX-CSP), *CrystEngComm*, 2024, **26**(35), 4782–4803, DOI: **10.1039/D3CE01306E**.

97 M. Baias, C. M. Widdifield, J.-N. Dumez, H. P. G. Thompson, T. G. Cooper, E. Salager, S. Bassil, R. S. Stein and L. Emsley, Powder Crystallography of Pharmaceutical Materials by Combined Crystal Structure Prediction and Solid-State 1H NMR Spectroscopy, *Phys. Chem. Chem. Phys.*, 2013, **15**(21), 8069, DOI: **10.1039/c3cp41095a**.

98 J. K. Harper and D. M. Grant, Enhancing Crystal-Structure Prediction with NMR Tensor Data, *Cryst. Growth Des.*, 2006, **6**(10), 2315–2321, DOI: **10.1021/cg060244g**.

99 C. S. Vojvodin, S. T. Holmes, L. K. Watanabe, J. M. Rawson and R. W. Schurko, Multi-Component Crystals Containing Urea: Mechanochemical Synthesis and Characterization by 35 Cl Solid-State NMR Spectroscopy and DFT Calculations, *CrystEngComm*, 2022, **24**(14), 2626–2641, DOI: **10.1039/D1CE01610E**.

100 J. Autschbach, S. Zheng and R. W. Schurko, Analysis of Electric Field Gradient Tensors at Quadrupolar Nuclei in Common Structural Motifs, *Concepts Magn. Reson., Part A*, 2010, **36A**(2), 84–126, DOI: **10.1002/cmr.a.20155**.

101 J. W. Akitt and W. S. McDonald, Arrangements of Ligands Giving Low Electric Field Gradients, *J. Magn. Reson.*, 1984, **58**(3), 401–412, DOI: **10.1016/0022-2364(84)90144-6**.

102 O. Knop, E. M. Palmer and R. W. Robinson, Arrangements of Point Charges Having Zero Electric-Field Gradient, *Acta Crystallogr.*, 1975, **31**(1), 19–31, DOI: **10.1107/S0567739475000046**.

103 O. Knop, Arrangements of Point Charges Having Zero Electric-Field Gradient, *Acta Crystallogr.*, 1976, **32**(1), 147–149, DOI: **10.1107/S0567739476000272**.

104 P. Pyykkö, Year-2017 Nuclear Quadrupole Moments, *Mol. Phys.*, 2018, **116**(10), 1328–1338, DOI: **10.1080/00268976.2018.1426131**.

105 D. A. Hirsh, A. J. Rossini, L. Emsley and R. W. Schurko, 35Cl Dynamic Nuclear Polarization Solid-State NMR of Active Pharmaceutical Ingredients, *Phys. Chem. Chem. Phys.*, 2016, **18**(37), 25893–25904, DOI: **10.1039/c6cp04353d**.

106 H. Hamaed, J. M. Pawlowski, B. F. T. T. Cooper, R. Fu, S. H. Eichhorn and R. W. Schurko, Application of Solid-State 35Cl NMR to the Structural Characterization of Hydrochloride Pharmaceuticals and Their Polymorphs, *J. Am. Chem. Soc.*, 2008, **130**(33), 11056–11065, DOI: **10.1021/ja802486q**.

107 J. A. Goedkoop and C. H. MacGillavry, IUCr, The Crystal Structure of Malonic Acid, *Acta Crystallogr.*, 1957, **10**(2), 125–127, DOI: **10.1107/S0365110X57000353**.

108 I. Tsivintzelis, G. M. Kontogeorgis and C. Panayiotou, Dimerization of Carboxylic Acids: An Equation of State Approach, *J. Phys. Chem. B*, 2017, **121**(9), 2153–2163, DOI: **10.1021/acs.jpcb.6b10652**.

109 R. Prohens, D. De Sande, M. Font-Bardia, A. Franconetti, J. F. González and A. Frontera, Gallic Acid Dimer As a Double Ï€-Hole Donor: Evidence from X-Ray, Theoretical Calculations, and Generalization from the Cambridge Structural Database, *Cryst. Growth Des.*, 2019, **19**(7), 3989–3997, DOI: **10.1021/acs.cgd.9b00387**.

110 H. C. S. Chan, G. R. Woollam, T. Wagner, M. U. Schmidt and R. A. Lewis, Can Picolinamide Be a Promising Cocrystal Former?, *CrystEngComm*, 2014, **16**(21), 4365–4368, DOI: **10.1039/C4CE00265B**.

111 I. S. Divya, S. Amrutha, S. Seethalekshmi and S. Varughese, Molecular Salts of Quinine: A Crystal Engineering Route to Enhance the Aqueous Solubility, *CrystEngComm*, 2021, **23**(39), 6942–6951, DOI: **10.1039/D1CE00791B**.

112 A. V. Trask, W. D. S. Motherwell and W. Jones, Physical Stability Enhancement of Theophylline via Cocrystallization, *Int. J. Pharm.*, 2006, **320**(1–2), 114–123, DOI: **10.1016/J.IJPHARM.2006.04.018**.

113 N. R. Jagannathan, S. S. Rajan and E. Subramanian, Refinement of the Crystal Structure of Malonic Acid, C3H4O4, *J. Chem. Crystallogr.*, 1994, **24**(1), 75–78, DOI: **10.1007/BF01665349**.

114 C. E. Hughes, G. N. M. Reddy, S. Masiero, S. P. Brown, P. A. Williams and K. D. M. Harris, Determination of a Complex Crystal Structure in the Absence of Single Crystals: Analysis of Powder X-Ray Diffraction Data, Guided by Solid-State NMR and Periodic DFT Calculations, Reveals a New 2′-Deoxyguanosine Structural Motif, *Chem. Sci.*, 2017, **8**(5), 3971–3979, DOI: **10.1039/C7SC00587C**.

115 C. A. O'Keefe, C. Mottillo, J. Vainauskas, L. Fábián, T. Friščić and R. W. Schurko, NMR-Enhanced Crystallography Aids Open Metal-Organic Framework Discovery Using Solvent-Free Accelerated Aging, *Chem. Mater.*, 2020, **32**(10), 4273–4281, DOI: **10.1021/acs.chemmater.0c00894**.

116 C. S. Vojvodin, S. T. Holmes, C. E. A. Kirschhock, D. A. Hirsh, I. H. Huskić, S. Senanayake, L. Betancourt, W. Xu and R. W. Schurko, Rietveld Refinement and NMR Crystallographic Investigations of Multicomponent Crystals Containing Alkali Metal Chlorides and Urea, *J. Appl. Crystallogr.*, 2025, **58**(2), 58, DOI: **10.1107/S1600576725001360**.

